

FPIC: a new Particle-In-Cell code for stationary and axisymmetric black-hole spacetimes

C. Meringolo  ¹ and L. Rezzolla  ^{1,2,3}

¹ Institut für Theoretische Physik, Goethe Universität, Max-von-Laue-Str. 1, D-60438 Frankfurt am Main, Germany

² School of Mathematics, Trinity College, Dublin 2, Ireland

³ Frankfurt Institute for Advanced Studies, Ruth-Moufang-Str. 1, 60438 Frankfurt am Main, Germany

February 10, 2026

ABSTRACT

Aims. Black holes in astrophysical environments are expected to be immersed in magnetized collisionless plasmas, whose electrodynamics leads to some of the powerful energetic emissions observed. To model such environments, a kinetic description is best-suited as it allows to capture the microphysics underlying the complex phenomena near such compact objects. In recent years, general-relativistic Particle-In-Cell (GRPIC) simulations have received increasing interest from the astrophysics community, becoming an excellent tool to study the immediate vicinity of the event horizons of stellar-mass and supermassive black holes. In this paper we present a newly developed GRPIC code framework called FPIC, providing a detailed description of the Maxwell-equations solver, of the particle “pushers”, and of the other algorithms that are needed in this approach.

Methods. Special attention is paid here to the fundamental issue of reproducibility and hence to a detailed discussion of the numerical methods employed and of the potential pitfalls that can be encountered in their implementation. We therefore describe in detail the code, which is written in Fortran and exploits parallel architectures using MPI directives both for the fields and particles. FPIC adopts spherical Kerr-Schild coordinates, which encode the overall spherical topology of the problem while remaining regular at the event horizon. The Maxwell equations are evolved using a finite-difference time-domain solver with a leapfrog scheme, while multiple particle “pushers” are implemented for the evolution of the particles. In addition to well-known algorithms, we introduce a novel hybrid method that dynamically switches between the most appropriate scheme based on the violation of the Hamiltonian energy.

Results. We first present results for neutral particles orbiting around black holes, both in the Schwarzschild and Kerr metrics, monitoring the evolution of the Hamiltonian error across different integration schemes. We apply our hybrid approach, showing that it is capable of achieving improved energy conservation at reduced computational cost. Results for charged particles in the presence of a magnetic field are also presented, where the interpolation plays a crucial role in maintaining Hamiltonian conservation. We then apply FPIC to investigate the Wald solution, first in electrovacuum and subsequently in plasma-filled configurations. In the latter case, particles with negative energy at infinity are present inside the ergosphere, indicating that the Penrose process is active. Finally, we present the split-monopole solution in a plasma-filled environment and successfully reproduce the Blandford-Znajek luminosity, finding very good agreement with analytical predictions.

Key words. Black hole physics - High energy astrophysics – Plasma astrophysics

1. Introduction

There is little doubt that black holes provide extreme physical conditions and whether at the centre of galaxies – as in the case of active galactic nuclei (AGNs) – or produced by the merger of neutron stars – as in the case of short gamma-ray bursts – they have long been considered responsible for the launching of powerful relativistic jets of plasma.

In the case of AGNs, the physics behind these extreme phenomena has been recently explored with the first images of the supermassive black holes M87* (Event Horizon Telescope Collaboration et al. 2019), and Sgr A* (Event Horizon Telescope Collaboration et al. 2022). Considerable effort has been dedicated over the last years to the modelling, via general-relativistic magnetohydrodynamics (GRMHD) simulations, of the accretion of plasma onto black holes (Del Zanna et al. 2020; Nathanail et al. 2022; Dihingia et al. 2022; Cruz-Osorio et al. 2022; Das et al. 2022; Fujibayashi et al. 2020; Dhruv et al. 2025; Megale et al. 2025; Pierre Jacques et al. 2025; Uniyal et al. 2025), so as to interpret the astronomical observations of the Event Horizon

Telescope Collaboration and extract physically relevant information. GRMHD simulations have also shown that rapidly spinning black holes threaded by a strong magnetic field can have its rotational energy extracted electromagnetically via the Blandford-Znajek process, launching powerful jets (Blandford & Znajek 1977; Tchekhovskoy et al. 2011; Koide & Arai 2008; McKinney et al. 2012; Asenjo & Comisso 2017; Comisso & Asenjo 2021; Camilloni & Rezzolla 2025).

Despite the overall success to reproduce the large-scale features of the accreting flow, one of the limitations of GRMHD simulations is that – in their most common implementation – they treat the plasma as a single fluid, only modelling the dynamically important part of the fluid, the protons – or, in general, the ions; (see Dihingia et al. 2022; Most et al. 2022; Gorard et al. 2025, for first attempts to two-species GRMHD simulations). Such a description leaves completely undetermined the microphysical properties of the electrons, such as their energy distribution, the number densities, and temperatures. This represents a significant limitation, since in hot, ionised jets around black holes, the Coulomb coupling between electrons and protons is inefficient, so that protons and elec-

trons are likely to have distinct temperatures, as it happens in the solar wind (Tu & Marsch 1997; van der Holst et al. 2010; Dihingia et al. 2022; Cruz-Osorio et al. 2025). To cope with this problem, a large number of *kinetic* Particle-In-Cell approaches have been used in special-relativistic flat spacetimes, modelling a small domain of plasmas around compact objects, where the curvature can be neglected (Cerutti et al. 2015; Sironi & Spitkovsky 2014; Werner et al. 2018; Zhdankin et al. 2019; Wong et al. 2020; Sironi et al. 2021; Meringolo et al. 2023; Imbrogno et al. 2024, 2025).

In response to the need of having a microscopical, kinetic description of the plasma also in regions of large curvature, such as those in the vicinity of black holes and neutron stars, a number of general-relativistic Particle-In-Cell (GRPIC) codes have been developed only in the recent few years, thanks to a combination of advances in numerical codes and computational power. The first global two-dimensional (2D) GRPIC simulations have been presented by Parfrey et al. (2019), making use of the GRZeltron code, which studied how a black hole immersed in an asymptotically uniform Wald magnetic field produces jets and extracts rotational energy according to the Blandford-Znajek mechanism. It was also shown that a variant of the Penrose process can also be activated, allowing particles with negative energy at infinity to extract energy from the black hole. The same code was used for a number of subsequent papers both in 2D (Crinquand et al. 2020, 2021; Bransgrove et al. 2021; El Mellah et al. 2022; Galishnikova et al. 2023; Niv et al. 2023; Vos et al. 2025) and in three-dimensional (3D) scenarios (Crinquand et al. 2022; El Mellah et al. 2023; Figueiredo et al. 2025). All of these studies have highlighted the richness of the plasma dynamics near rotating black holes and the effectiveness of GRPIC simulations to model processes such as the disc accretion of magnetically dominated flows and the powering of relativistic jets.

Another GRPIC code that has been recently developed and is publicly available is Aperture (Chen et al. 2025), which was applied to study spark gaps and plasma injection in black hole magnetospheres, finding that the location and time evolution of the gap depend on the observer. Further works with this code are the self-consistent treatment of inverse Compton scattering with the inclusion of pair production (Yuan et al. 2025), and the study of kinetic equilibria of collisionless tori around a Kerr black hole that are stable in 2D axisymmetric simulations in the absence of and initial seed magnetic field (Luepker et al. 2026). Additional works in this direction are those presented by Hirotani et al. (2021), who developed a simplified GRPIC approach evolving only three electromagnetic-field components to study an axisymmetric magnetosphere around a rotating black hole and the recent contribution by Galishnikova et al. (2025), who presented the open-source, coordinate-agnostic GRPIC code Entity.

In this paper, we present a newly developed GRPIC code, FPIC, for stationary and axisymmetric black hole spacetimes. One of the major goals of this paper is to ensure reproducibility of scientific results. As a result, special attention is paid to a detailed discussion of the numerical methods employed in FPIC, and to the discussion of the potential difficulties that can be encountered when developing a GRPIC code from scratch. However, this is not a code-description paper only. In addition to the discussion of well-known numerical aspects and of standard code benchmarks, we also present a novel and more efficient method for the evolution of the charged particles and an astrophysical application to the study of the Blandford-Znajek process in a split-monopole magnetic topology.

The paper is organised as follows. In Section 2, we introduce the key ingredients of a GRPIC code and describe the

main algorithms implemented in FPIC. In Section 3, we present a series of simulations in order to validate the code. We begin with single-particle trajectories around Schwarzschild and Kerr black holes, introducing a new hybrid integrator. We then present results for rotating black holes immersed in Wald and split-monopole magnetic-field configurations. Finally, in Section 4, we summarise the results and discuss the main properties of the code. Hereafter, we employ Greek letters for tensor components in a four-dimensional manifold and Latin letters for the corresponding spatial components. We also adopt the summation convention on repeated indices and geometrised units (see, e.g., Rezzolla & Zanotti 2013).

2. The GRPIC algorithm

FPIC models the dynamics of charged particles in a stationary and axisymmetric spacetime, described by the black hole mass $M = 1$ and by the dimensionless spin parameter $0 \leq a_* \leq 1$, being $a_* := J_*/M^2$ and J_* the spin angular momentum of the spacetime. The code employs the standard 3+1 spacetime decomposition (Thorne & Macdonald 1982; Komissarov 2004), where the line element is described by:

$$ds^2 = -\alpha^2 dt^2 + \gamma_{ij}(dx^i + \beta^i dt)(dx^j + \beta^j dt). \quad (1)$$

As usual, the three-metric is represented by γ_{ij} , while α and β^i refer to the lapse function and the shift vector, respectively (Rezzolla & Zanotti 2013). To ensure regularity at the black hole horizon, the metric is expressed in terms of the spherical Kerr-Schild coordinates (t, r, θ, φ) , because these encode the spherical symmetry of the problem and remain regular at the event horizon (see Appendix A for details). All the fields are invariant by rotation around the spin axis of the black hole, i.e., $\partial_\varphi \psi(r, \theta) = 0$ for all quantities ψ in the code. In that sense, although particles move in a full 3D space, the fields are defined by 2D arrays, being often called “2.5D” approximation. Hereafter, and unless specified differently, we use geometrised units in which $c = 1 = G$, with c and G the speed of light and the gravitational constant, respectively.

2.1. Maxwell Equations Solver

For static electromagnetic fields, the covariant antisymmetric Maxwell tensor can be expressed in terms of derivatives of the four-potential A_μ , as

$$F_{\mu\nu} = g_{\mu\alpha} g_{\nu\beta} F^{\alpha\beta} = \partial_\mu A_\nu - \partial_\nu A_\mu. \quad (2)$$

FPIC evolves the contravariant electric field D^i and magnetic field B^i as dynamic variables as measured by a fiducial observer (FIDO), defined by (Komissarov 2004; Mizuno & Rezzolla 2024)

$$D^i = \alpha F^{0i}, \quad B^i = \alpha^* F^{i0}, \quad (3)$$

where we have defined the dual of the Maxwell tensor

$${}^*F_{\mu\nu} := \sqrt{-g} \eta_{\mu\nu\alpha\beta} F^{\alpha\beta}, \quad (4)$$

being $\eta_{\mu\nu\alpha\beta}$ the completely anti-symmetric Levi-Civita symbol. The general-relativistic Maxwell equations in a stationary metric can be written as (Baumgarte & Shapiro 2010;

Rezzolla & Zanotti 2013):

$$\frac{1}{\sqrt{\gamma}} \partial_j (\sqrt{\gamma} D^j) = 4\pi \rho, \quad (5)$$

$$\frac{1}{\sqrt{\gamma}} \partial_j (\sqrt{\gamma} B^j) = 0, \quad (6)$$

$$\frac{1}{\sqrt{\gamma}} \eta^{ijk} \partial_j H_k - 4\pi J^i = \partial_t D^i, \quad (7)$$

$$-\frac{1}{\sqrt{\gamma}} \eta^{ijk} \partial_j E_k = \partial_t B^i, \quad (8)$$

where $\mathbf{J} := \alpha \mathbf{j} - \rho \boldsymbol{\beta}$, \mathbf{j} is the current density as measured by FIDOs and $\eta_{ijk} = \eta^{ijk}$ is the 3-dimensional Levi-Civita symbol. Note that Eqs. (5)–(6) are simply constraints and are not evolved during the simulations. The evolution equations (7) and (8) refer to FIDO quantities but make use of the electric field \mathbf{E} and the magnetic field \mathbf{H} as measured from the grid, where:

$$H_i = \frac{1}{2} \alpha \sqrt{\gamma} \eta_{ijk} F^{jk} = \alpha B_i - \sqrt{\gamma} \eta_{ijk} \beta^j D^k, \quad (9)$$

$$E_i = F_{i0} = \alpha D_i + \sqrt{\gamma} \eta_{ijk} \beta^j B^k. \quad (10)$$

We make use of the Yee grid (Yee 1966), where all the electromagnetic fields are staggered and located in different grid positions (Cerutti et al. 2015; Torres et al. 2024), as sketched in Fig. 1. One of the major benefits of employing the Yee grid is that Eq. (6) is automatically satisfied to machine round-off precision, provided the simulation is initialised with a divergence-less magnetic field, i.e., $\partial_t [\partial_j (\sqrt{\gamma} B^j) / \sqrt{\gamma}] = 0$.

The code solves the time-dependent Maxwell equations (7) and (8) via a time-centered leapfrog scheme (Isersles 1986; Birdsall & Langdon 2005). Electric and magnetic fields are staggered not only in space, but also in time. The code knows \mathbf{B} and \mathbf{H} at integer time steps n and $n+1$, while electric fields \mathbf{D} and \mathbf{E} are stored at semi-integers timesteps $n+1/2$ and $n+3/2$. In order to evolve electromagnetic fields and particles, the following sub-steps are employed (Crinqueand 2021; Galishnikova et al. 2025):

1. Compute $\mathbf{E}^{n+1} = \alpha(\mathbf{D})^{n+1} + \boldsymbol{\beta} \times \mathbf{B}^{n+1}$;
2. Evolve $\langle \mathbf{B} \rangle^{n+1/2}$ to $\mathbf{B}^{n+3/2}$ via Eq. (8) and \mathbf{E}^{n+1} ;
3. Compute $\mathbf{E}^{n+3/2} = \alpha \mathbf{D}^{n+3/2} + \boldsymbol{\beta} \times \mathbf{B}^{n+3/2}$;
4. Evolve \mathbf{B}^{n+1} to \mathbf{B}^{n+2} via Eq. (8) and $\mathbf{E}^{n+3/2}$;
5. Push particles at \mathbf{x}^{n+1} and four-velocity \mathbf{u}^{n+1} to $(\mathbf{x}, \mathbf{u})^{n+2}$ with $\mathbf{B}^{n+3/2}, \mathbf{D}^{n+3/2}$;
6. Update source terms $\rho^{n+2}, \mathbf{J}^{n+2}$;
7. Compute $\mathbf{H}^{n+3/2} = \alpha \mathbf{B}^{n+3/2} - \boldsymbol{\beta} \times \mathbf{D}^{n+3/2}$;
8. Evolve \mathbf{D}^{n+1} to \mathbf{D}^{n+2} via Eq. (7) and $\mathbf{H}^{n+3/2}, \langle \rho \rangle^{n+3/2}, \langle \mathbf{J} \rangle^{n+3/2}$;
9. Compute $\mathbf{H}^{n+2} = \alpha \mathbf{B}^{n+2} - \boldsymbol{\beta} \times \mathbf{D}^{n+2}$;
10. Evolve $\mathbf{D}^{n+3/2}$ to $\mathbf{D}^{n+5/2}$ via Eq. (7) and $\mathbf{H}^{n+2}, \mathbf{J}^{n+2}$,

where $\langle \psi \rangle^n = (\psi^{n-1/2} + \psi^{n+1/2})/2$ indicates an average between different timesteps. Note that, to preserve the leapfrog scheme, we need to 1) store the fields D^i, B^i, J^i and ρ at two different timesteps, and 2) double the ordinary leapfrog pushes, in order to evolve the fields. In addition to this, a number of other numerical subtleties are hidden when coupling FIDOs and non-FIDOs

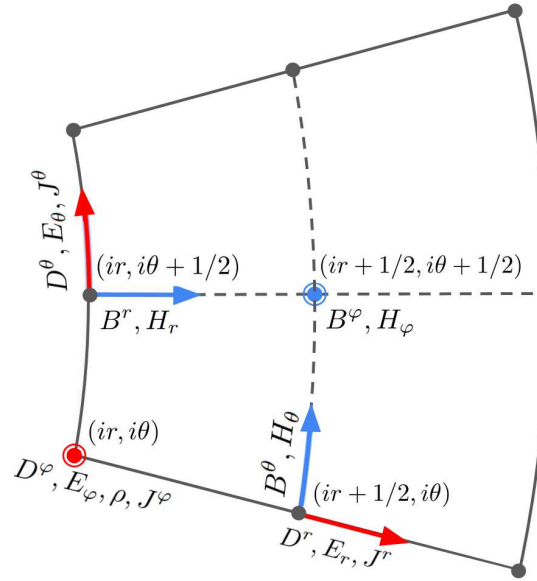


Fig. 1: Spherical Yee grid adopted in FPIC. The red arrows denote the components of the electric fields \mathbf{D}, \mathbf{E} , and the current density \mathbf{J} , the blue ones denote the magnetic fields \mathbf{B}, \mathbf{H} . The positions on the mesh are labelled by the indices ir in the radial direction and $i\theta$ in the radial direction. Note that at $(ir, i\theta)$ and $(ir + 1/2, i\theta + 1/2)$ the vectors are pointing outwards.

quantities living in different Yee-grid points. To see this, we can consider, for example, the radial component of Eq. (7), which reads $\partial_t D^r = (\partial_\theta H_\phi) / \sqrt{\gamma} - 4\pi J^r$. To solve this equation, we need $H_\phi = \alpha B_\phi - \sqrt{\gamma} \beta^r D^r$, but note from Fig. 1 that B_ϕ and D^r are located at different grid positions. Also, we need to compute the covariant component $B_\phi = \gamma_{i\phi} B^i$, where again, different components need to be centered in space. As an example, to obtain the B^r component at the same grid position of the B^ϕ component, i.e. at $(ir + 1/2, i\theta + 1/2)$, we perform the following metric-weighted linear interpolation:

$$B_{(ir+1/2,i\theta+1/2)}^r = \frac{(\sqrt{\gamma} B^r)_{(ir,i\theta+1/2)} + (\sqrt{\gamma} B^r)_{(ir+1,i\theta+1/2)}}{2 \sqrt{\gamma}_{(ir+1/2,i\theta+1/2)}}. \quad (11)$$

Since such hidden calculations are ubiquitous for the evolution of electromagnetic fields, all the stationary metric components ($\alpha, \beta^i, \gamma_{ij}$ and $\sqrt{\gamma}$) are computed only initially and stored in all the different Yee grid points.

2.2. Particle Pusher

FPIC evolves the contravariant three-coordinate x^i and the covariant momentum vector u_i as dynamic variables for the particles. In the 3 + 1 formalism and stationary metrics, the Hamiltonian for a charged particle under the electromagnetic and gravitational forces reads

$$H(x^i, u_j) = \alpha \Gamma - \beta^k u_k - \frac{q}{m} A_0, \quad (12)$$

where $\Gamma := \sqrt{1 + \gamma^{ij} u_i u_j}$ is the particle Lorentz factor measured by a FIDO, m is the mass of the particle, $q = \pm e$ the charge, and A_0 is the time-component of the four-vector potential A_μ . The general-relativistic equations of motion for the position and the four-velocity of the particles can be obtained by differentiating

H such that (Bacchini et al. 2019):

$$\frac{dx^i}{dt} = \frac{\partial H}{\partial u_i} = \frac{\alpha}{\Gamma} \gamma^{ij} u_j - \beta^i, \quad (13)$$

$$\frac{du_i}{dt} = -\frac{\partial H}{\partial x^i} = \mathcal{A}_i^{(g)} + \mathcal{A}_i^{(em)}, \quad (14)$$

where the two acceleration terms in the evolution of momentum can be written as:

$$\mathcal{A}_i^{(g)} = -\Gamma \partial_i \alpha + u_j \partial_i \beta^j - \frac{\alpha}{2\Gamma} u_i u_m \partial_i \gamma^{lm}, \quad (15)$$

$$\mathcal{A}_i^{(em)} = \frac{q\alpha}{m} \left[\gamma_{ij} D^j + \frac{\sqrt{\gamma} \eta_{ijk} \gamma^{jl} u_l B^k}{\Gamma} \right]. \quad (16)$$

To increase the accuracy of the pusher, both the metric components in Eqs. (13)–(16) and their derivatives are computed analytically at the position of the particle.

FPIC implements different schemes to solve the above evolution equations for particles: 1) an explicit fourth-order Runge-Kutta (RK4) integrator (Press et al. 1992); 2) an implicit midpoint rule (IMR) (Feng 1986); 3) a second-order implicit Hamiltonian method (Bacchini et al. 2018). The two implicit methods, i.e., the IMR and the Hamiltonian methods, are the most accurate ones, but also computationally demanding, while the RK4 scheme shows acceptable results in terms of accuracy at a fraction of the computational cost. As a result, although the RK4 integrator is not symplectic, i.e., the area of a given region of the phase space is not guaranteed to be preserved over long timescales, (as required by Liouville’s theorem (Rezzolla & Zanotti 2013)), it has represented for us the optimal approach in terms of accuracy and computational costs for most of the cases we considered.

Once the updated positions and velocities are computed, the new charge and current density are then moved from the sources to the Yee grid via a metric-weighted 2D linear interpolation, as discussed in detail in the next Subsections.

2.2.1. Runge-Kutta 4 integrator

The fourth-order RK4 scheme is a classical explicit integrator commonly used in scientific community for the numerical solution of ordinary differential equations (ODEs) (Press et al. 1992). A key advantage of this method is that it updates the solution through a fixed sequence of non-iterative stages. Considering a generic function $f^n(\mathbf{x}, t)$, representing the time-discretized form of an ODE problem at time n , we can write:

$$\frac{f^{n+1} - f^n}{\Delta t} = \mathcal{F}(t, f), \quad (17)$$

where $\mathcal{F}(t, f)$ is a given function. For each timestep, the RK4 scheme corresponds to first recursively calculating the following quantities

$$k_1 = \Delta t \mathcal{F}(t^n, f^n), \quad (18)$$

$$k_2 = \Delta t \mathcal{F}(t^n + \Delta t/2, f^n + k_1/2), \quad (19)$$

$$k_3 = \Delta t \mathcal{F}(t^n + \Delta t/2, f^n + k_2/2), \quad (20)$$

$$k_4 = \Delta t \mathcal{F}(t^n + \Delta t, f^n + k_3), \quad (21)$$

and finally advances the variable $f(t)$ by means of

$$f^{n+1} = f^n + \frac{1}{6} (k_1 + 2k_2 + 2k_3 + k_4). \quad (22)$$

Notice that the RK4 scheme requires four evaluations of the sources to advance one timestep, and the resulting error in $f(t)$ in the computed solution is of order $O(\Delta t^5)$. The main drawback of explicit methods, such as the RK4 scheme, is that they are generally unable to preserve the first integrals of motion, when these exist. Moreover, explicit integrators do not conserve the phase space volume, in other words, they are non-symplectic schemes (Hairer et al. 2002). As a consequence, in addition to the truncation errors of a given order in the solution variable $f(t)$, other errors may inevitably accumulate and grow over long-time integrations.

However, the scaling of the errors with decreasing timestep Δt is satisfactory enough to be generally acceptable for the RK4 method. As we will show in the following Sections, this scheme provides the best compromise between computational cost and accuracy, while preserving energy conservation within acceptable values over the typical time scales of GRPIC simulations. Further improvements for the RK4 method can be obtained by adopting adaptive timestep control, but they can increase the overall computational cost of the simulation, and we usually adopt a fixed timestep unless specified differently.

2.2.2. Implicit Midpoint Rule

The implicit midpoint rule (IMR) is the simplest symplectic integrator, and it is second-order accurate (Feng 1986; Bacchini et al. 2018). It solves ordinary differential equations $\partial_t y = f(y)$ according to

$$\frac{f^{n+1} - f^n}{\Delta t} = \mathcal{F}(t^{n+1/2}, f^{n+1/2}), \quad (23)$$

where in the right hand side we estimate $f^{n+1/2} = (f^n + f^{n+1})/2$. Note that this is an implicit method, since f^{n+1} is our unknown, but it appears on both sides of Eq. (23). We solve iteratively the above equation, including both the terms $\mathcal{A}_i^{(em)}$ and $\mathcal{A}_i^{(g)}$ for charged particles. We update f^{n+1} for the k -th iteration according to

$$f^{n+1,[k]} = f^n + \frac{\Delta t}{2} \mathcal{F}(f^n + f^{n+1,[k-1]}). \quad (24)$$

We employ a classical Newton iterative scheme (Press et al. 1992), which usually converges to the machine round-off after $k \sim 10$ –15 iterations for all the six components (x^i, u_j). The IMR has a higher cost than the RK4 integrator, but it has the benefits of unconditional stability and of being symplectic. The Hamiltonian energy is not conserved exactly, but the error is bounded in time and of order $O(\Delta t^3)$. Moreover, the implicit nature of this scheme allows for larger Δt without compromising stability (Birdsall & Langdon 2005).

2.2.3. Hamiltonian integrator

In some particular cases, one may need a scheme that does exactly conserve energy, such as the second-order, Hamiltonian-preserving scheme (Bacchini et al. 2018, 2019). It is straightforward to show that, in the continuous case, the variation of the Hamiltonian vanishes by application of the chain rule

$$\frac{\partial H(x^i, u_j)}{\partial t} = \frac{\partial H}{\partial x^i} \frac{dx^i}{dt} + \frac{\partial H}{\partial u_j} \frac{du_j}{dt} = -\frac{du_i dx^i}{dt} + \frac{dx^i du_i}{dt} = 0. \quad (25)$$

The discretized formulation of Eq. (25) accordingly reads

$$\frac{\Delta H}{\Delta u_i} = \frac{\Delta x^i}{\Delta t}, \quad \frac{\Delta H}{\Delta x^i} = -\frac{\Delta u_i}{\Delta t}, \quad (26)$$

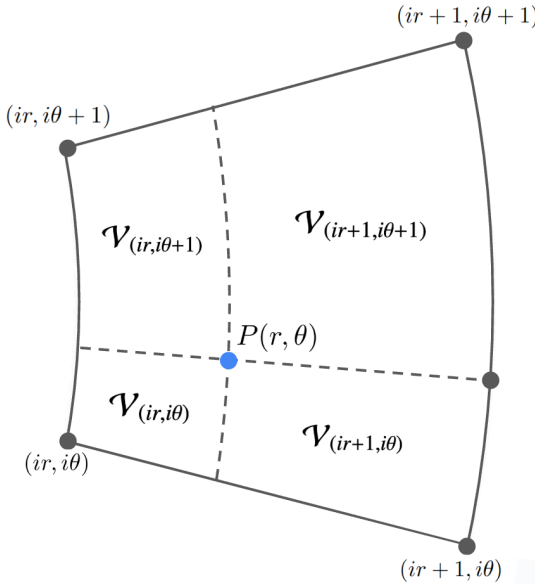


Fig. 2: Volume weighting procedure utilised in FPIC. Reported in the diagram is the geometry of a single cell in a 2D axisymmetric spherical mesh, with a particle located in the cell at position $P(r, \theta)$ (blue point). The volumes \mathcal{V} involved in the interpolation scheme are also reported, accordingly.

and will in principle satisfy $\Delta H/\Delta t = 0$ under certain conditions. Since the Hamiltonian is a function of six variables, we must treat carefully the differentiation with respect to each variable. Here we follow the approach of Bacchini et al. (2018), defining \mathcal{H} the Hamiltonian containing some average relative to the variables that are not differentiated, rewriting Eqs. (26) as

$$\frac{x_i^{i,n+1} - x_i^{i,n}}{\Delta t} = \frac{\mathcal{H}(\mathbf{x}, u_i^{n+1}, u_l, u_m) - \mathcal{H}(\mathbf{x}, u_i^n, u_l, u_m)}{u_i^{n+1} - u_i^n}, \quad (27)$$

$$\frac{u_i^{n+1} - u_i^n}{\Delta t} = \frac{\mathcal{H}(x^{i,n+1}, x^l, x^m, \mathbf{u}) - \mathcal{H}(x^{i,n}, x^l, x^m, \mathbf{u})}{x^{i,n+1} - x^{i,n}}, \quad (28)$$

and reporting the details in Appendix D. Note that this scheme is completely generic and can be applied to different physical situations provided that the corresponding Hamiltonian $H(x^i, u_j)$ is available, and retaining first integrals conservation properties. However, despite this pusher is the most accurate among all the ones implemented, it remains unfeasible when evolving a large number of particles as expected by a PIC code, because of its high computational cost. In FPIC we implemented the Hamiltonian formalism only for the geodesic motion, as presented in Bacchini et al. (2018), remaining overall a very good particle pusher for a few test-particle cases and testbeds, when only the $\mathcal{A}_i^{(g)}$ term is present.

2.3. Current and charge deposition

The deposition of currents and charges is an important step for PIC codes. To update the Ampère-Maxwell law in Eq. (7), the source terms ρ and \mathbf{J} are needed, capturing the coupling between the electromagnetic fields and the charged particles. FPIC uses a 2D linear interpolation to deposit the charge from the particles into each grid node. The proportion of a charge which is deposited on a given node is determined by the volume defined by the position of the particle between the four grid points of the cell.

It is worth mentioning that in PIC simulations each particle is assigned a numerical weight w , which compensates for the low number of numerical particles used in kinetic simulations compared to the actual number of particles in real astrophysical plasmas (Birdsall & Langdon 2005). As a result, a single numerical particle represents a large number of physical particles with the same charge-to-mass ratio and following identical phase-space trajectories (for this reason, they are also referred to as *macroparticles*).

Consider a single particle located at the point $P(r, \theta)$ (see the blue point in Fig. 2), which has charge q and weight w , and is located between nodes $r_{ir} \leq r \leq r_{ir+1}$ and $\theta_{i\theta} \leq \theta \leq \theta_{i\theta+1}$. The charge deposited on each node is computed as

$$q_{(ir,i\theta)} = \frac{\mathcal{V}_{(ir,i\theta+1)}}{\mathcal{V}} qw, \quad (29)$$

$$q_{(ir+1,i\theta)} = \frac{\mathcal{V}_{(ir,i\theta+1)}}{\mathcal{V}} qw, \quad (30)$$

$$q_{(ir,i\theta+1)} = \frac{\mathcal{V}_{(ir+1,i\theta)}}{\mathcal{V}} qw, \quad (31)$$

$$q_{(ir+1,i\theta+1)} = \frac{\mathcal{V}_{(ir,i\theta)}}{\mathcal{V}} qw, \quad (32)$$

where \mathcal{V} is the total volume between the four grid nodes, given by

$$\mathcal{V} = \int_{r_{ir}}^{r_{ir+1}} \int_{\theta_{i\theta}}^{\theta_{i\theta+1}} \sqrt{\gamma} dr d\theta. \quad (33)$$

The other *subvolumes* in the cell are computed according to

$$\mathcal{V}_{(ir,i\theta)} = \int_{r_{ir}}^r \int_{\theta_{i\theta}}^{\theta} \sqrt{\gamma} dr d\theta, \quad (34)$$

$$\mathcal{V}_{(ir+1,i\theta)} = \int_r^{r_{ir+1}} \int_{\theta_{i\theta}}^{\theta} \sqrt{\gamma} dr d\theta, \quad (35)$$

$$\mathcal{V}_{(ir,i\theta+1)} = \int_{r_{ir}}^r \int_{\theta}^{i\theta+1} \sqrt{\gamma} dr d\theta, \quad (36)$$

$$\mathcal{V}_{(ir+1,i\theta+1)} = \int_r^{r_{ir+1}} \int_{\theta}^{i\theta+1} \sqrt{\gamma} dr d\theta. \quad (37)$$

Note that, even if the geometry is 2D, the determinant of the metric in Eqs. (33)–(37) is fully 3D, and is reported in Eq. (A.4). We evaluate the different volumes via numerical integration by using the 2D trapezoidal rule, and discretising each cell into 4×4 points in r and θ .

The total charge density ρ and current density \mathbf{J} deposited at the grid point $(ir, i\theta)$, for instance, reads:

$$\rho_{(ir,i\theta)} = \sum_k \frac{w^k q_{(ir,i\theta)}^k \mathcal{V}_{(ir+1,i\theta+1)}^k}{\mathcal{V}^k}, \quad (38)$$

$$\mathbf{J}_{(ir,i\theta)} = \sum_k \frac{w^k q_{(ir,i\theta)}^k v_{(ir,i\theta)}^k \mathcal{V}_{(ir+1,i\theta+1)}^k}{\mathcal{V}^k}, \quad (39)$$

where the sum is considered over all the k particles located into the volume \mathcal{V} , and $v^j = \gamma^{ij} u_i / \Gamma$ is the particle's three-velocity measured by FIDOs. In a similar way, one can compute the charge and current densities on the other Yee grid nodes.

2.4. Divergence cleaning

The Yee algorithm guarantees that the divergence-free constraint on the magnetic field is preserved exactly in time, i.e.,

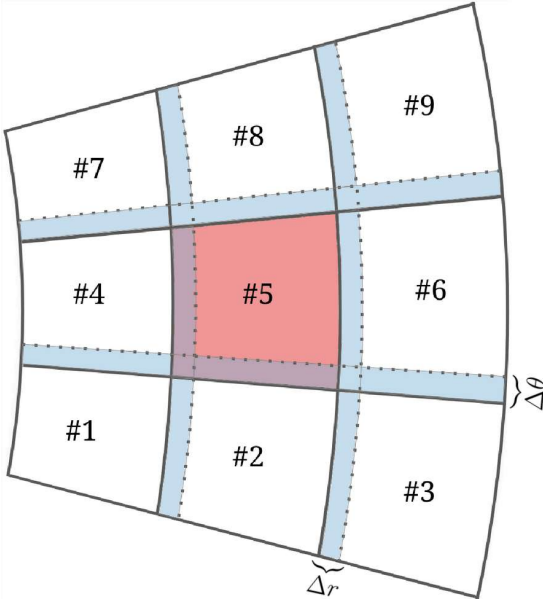


Fig. 3: MPI-domain decomposition scheme employed in FPIC. The diagram shows a portion of the computational domain with 9 CPUs, where solid black lines delimit the *physical* sub-domains assigned to each CPU. Each *computational* sub-domain extends beyond the physical one by Δr (radial direction) and $\Delta\theta$ (angular direction) to allow MPI communications, and CPUs exchange information with the neighbours across the light-blue shaded regions.

$\partial_t(\nabla \cdot \mathbf{B}) = 0$, provided it is satisfied initially. In contrast, Gauss law for the electric displacement field, $\nabla \cdot \mathbf{D} = 4\pi\rho$, is not automatically preserved in the presence of charged particles, unless the current deposition scheme satisfies the discrete charge continuity equation exactly. As a consequence, numerical errors in $\nabla \cdot \mathbf{D}$ may accumulate over time and require explicit correction.

To enforce Gauss's law, we periodically perform divergence cleaning by solving the Poisson equation

$$\frac{1}{\sqrt{\gamma}} \partial_k \left(\sqrt{\gamma} \gamma^{kl} \partial_l \phi \right) = \frac{1}{\sqrt{\gamma}} \partial_j \left(\sqrt{\gamma} D^j \right) - 4\pi\rho, \quad (40)$$

and correcting the electric field according to $D_{\text{new}}^i = D_{\text{old}}^i - \gamma^{ij} \partial_j \phi$. In FPIC, Eq. (40) is solved using an iterative Jacobi method. We usually update the correct electric field every 25 timesteps, solving Eq. (40) with 500 iterations, but these values can change depending the physical setup employed.

2.5. Boundary conditions

Thanks to the properties of the Kerr-Schild coordinates, the inner radial boundary is set to be within the event horizon, which lies in a region causally disconnected from the rest of the domain, and here we enforce a zero-gradient constraint on the dynamical variables $\partial_r \mathbf{D} = \partial_r \mathbf{B} = 0$. At the outer boundary of the radial domain, we aim to mimic open boundaries, namely perfectly absorbing boundaries with no reflection of waves and particles, thus isolating the system from the external environment. In practice, we add an artificial dissipative term to Maxwell's equations to exponentially damp the fields in a spherical shell located at

the outer regions of the box, according to (Cerutti et al. 2015)

$$\partial_t \mathbf{B} = -\nabla \times \mathbf{E} - \chi(r) \mathbf{B}, \quad (41)$$

$$\partial_t \mathbf{D} = \nabla \times \mathbf{H} - 4\pi \mathbf{J} - \chi(r) \mathbf{D}, \quad (42)$$

where $\chi(r)$ is the conductivity of the absorbing region and reads

$$\chi(r) = \chi_0 \left(\frac{r - r_{\text{abs}}}{r_{\text{max}} - r_{\text{abs}}} \right)^\lambda. \quad (43)$$

Typical values are $r_{\text{abs}} = 0.9 r_{\text{max}}$, $\chi_0 = 10^4$, and $\lambda = 5$, but they may vary slightly across different setups.

The θ -domain can assume two geometries: the *full*- θ domain, covering the range $0 \leq \theta \leq 2\pi$, and the *half*- θ domain, extending from the south pole ($\theta_0 = 0$) to the north pole ($\theta_{\text{max}} = \pi$). The field and particle boundary conditions change accordingly: In the *full*- θ configuration, we simply apply periodic boundary conditions at $\theta_{\text{max}} = 2\pi$; for the *half*- θ configuration we apply the axial symmetry to all Yee field components located on the boundaries θ_0 and θ_{max} , i.e., $\partial_r D^r = D^\theta = B^\theta = 0$. To avoid numerical issues when θ approaches the poles, we set $\theta_0 = \epsilon$ and $\theta_{\text{max}} = \pi - \epsilon$, typically with $\epsilon = \pi/200$. Similarly, in the *full*- θ geometry, we set $\theta_0 = \epsilon$ and $\theta_{\text{max}} = 2\pi + \epsilon$, with $\epsilon = \pi/(2N_\theta)$, ensuring that the poles lie midway between two Yee-grid points.

Particles falling into the black hole ($r < r_h$) or reaching the outer boundary ($r > r_{\text{max}}$) are removed from the simulation. They are reflected upon passing across the poles for the *half*- θ domain configuration (i.e., with u_θ changing sign at the poles), while they follow periodic boundary conditions for the *full*- θ configuration.

2.6. Parallelisation

FPIC implements a grid-based domain decomposition applied through the MPI directives, which ensures the communication among the different processors. The global simulation box is described by $N_r \times N_\theta$ grid points, divided into a number of CPUs given by $N^{\text{cpu}} = N_r^{\text{cpu}} \times N_\theta^{\text{cpu}}$, where the latter refer to the CPUs along the r - and θ - directions, respectively. In a spherical 2D decomposition, the bulk domains have 8 neighbours (see Fig. 3 for a schematic representation). Each of the N CPUs is assigned to a portion of the entire domain, evolving the fields and pushing the particles that propagate within its proper sub-domain, given by $(N_r/N_r^{\text{cpu}} + 1) \times (N_\theta/N_\theta^{\text{cpu}} + 1)$. The “+ 1” refers to the so-called *ghost cells* (the blue shaded regions in Fig. 3), which are needed for communication among neighbours. This means that the domains overlap in such a way that they share common cells, so that neighbour CPUs can exchange information such as which particles have left or entered their domain, and what the updated values of the fields are at the boundaries of the domain. The latter is used, for instance, when computing derivatives at the edges of each sub-domain.

3. Code Validation

In this Section we aim to test the FPIC code through a series of numerical testbeds. We start by validating the particle pushers by integrating the trajectories of neutral particles under the influence of the gravitational field of the black hole only. Then we evolve the dynamics of charged test-particles when immersed in a stationary Wald magnetic field, monitoring the conservation of the Hamiltonian energy. Finally, we test the Maxwell equations solver both in electrovacuum and in a plasma-filled scenario, by using a Wald and a split-monopole configuration.

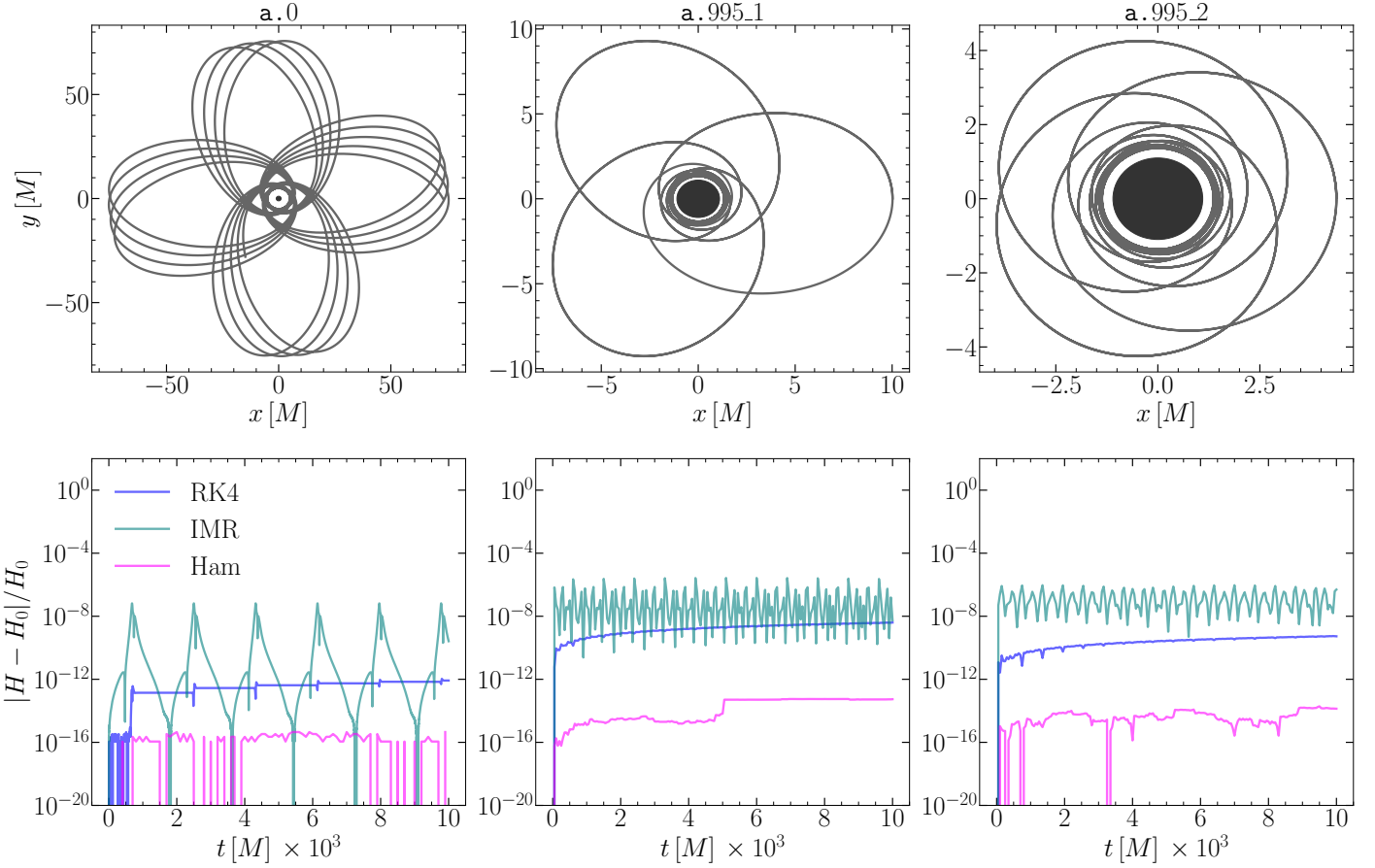


Fig. 4: Top row: orbits in the (r, φ) plane for neutral particles around black holes. The black disk at the center of each panel represents the horizon; Bottom row: deviation of energy from its original value, $|H - H_0|/H_0$, vs time for each case. From left to right: a few precessing orbits for the “four-leaf” orbit with $E = 0.987649$ and $L = 3.9$ around a Schwarzschild black hole; orbits around Kerr black hole with $a_* = 0.995$, and $\{E, L\} = \{0.916235, 2\}, \{0.841423, 1.82\}$, respectively (see the Tab. C.1 for details). We report the energy errors for the RK4 (blue), the IMR (teal), and the Hamiltonian (magenta) schemes, up to $t = 10^4 M$.

3.1. Test Particle Trajectories

3.1.1. Neutral particles

We integrate the paths of particles around black holes to test particle solvers implemented in FPIC. As a first testbed, we consider only the geodesic solver, in the absence of any electromagnetic field. We have selected three particular paths for neutral particles (i.e., $q = 0$ in Eq. (16)) both in Schwarzschild and Kerr metrics (Levin & Perez-Giz 2008; Bacchini et al. 2018; Chen et al. 2025) (for details of physical and numerical parameters, see the Tab. C.1). The particle’s motion lies in the equatorial plane, at $\theta_0 = \pi/2$, with vanishing u_θ . Among the three orbits, the first one is for a Schwarzschild black hole, while the others refer to a Kerr black hole with spin $a_* = 0.995$. Correctly reproducing these trajectories is a first but important testbed for the particle pushers implemented in FPIC, being a test of long-time stability thanks to the periodicity of orbits. For these tests only the term \mathcal{A}_g acts on the particle, and we compute the metric components and their derivatives analytically, directly on the particle position. Since no interpolations are needed, the number of mesh points do not play any role on the accuracy of the simulations. The timestep is fixed to $\Delta t = 10^{-1}$ for all the three orbits.

In the top row of Fig. 4 we report the particle trajectories which are produced with FPIC, and integrated up to $t = 10^4 M$. Note that the trajectory around the Schwarzschild black hole slowly precesses and close up on itself after approximately 1000

cycles (we report only a few circles of the trajectory), while for the orbits around Kerr black holes we report the full trajectories up to $t = 10^4 M$. The panels in the bottom row show the evolution of $|H(t) - H_0|/H_0$ accordingly, where $H = -u_0$ is the conserved energy and H_0 is the initial energy. The different colours refer to different integrators, highlighting that the Hamiltonian scheme is the most accurate among the others. The RK4 and the IMR method show higher violation of energy, but the error is overall small and stable up to long timescales. All the schemes show a good conservation of the energy over the entire duration of integration for all the particle trajectories, and are consistent with other approaches in the literature (Levin & Perez-Giz 2008; Bacchini et al. 2018; Chen et al. 2025). Even if the RK4 scheme is non-symplectic, it is the faster one among the 3 integrators, and we measured $t_{\text{IMR}}/t_{\text{RK4}} \sim 2.15$ and $t_{\text{Ham}}/t_{\text{RK4}} \sim 41.2$, where $t_{\#}$ refer to the time needed to reach $t = 10^4 M$ for each scheme.

3.1.2. Hybrid integration scheme

As we have seen, the Hamiltonian scheme is very computationally demanding, but it is able to retain extremely low values of errors. Conversely, the RK4 integrator is much faster, though at the price of a larger error violation. In particular, the bottom-left panel of Fig. 4 shows an interesting behavior in the RK4 error evolution: the violation remains almost constant in time, except at a few specific moments, i.e., when the particle approaches

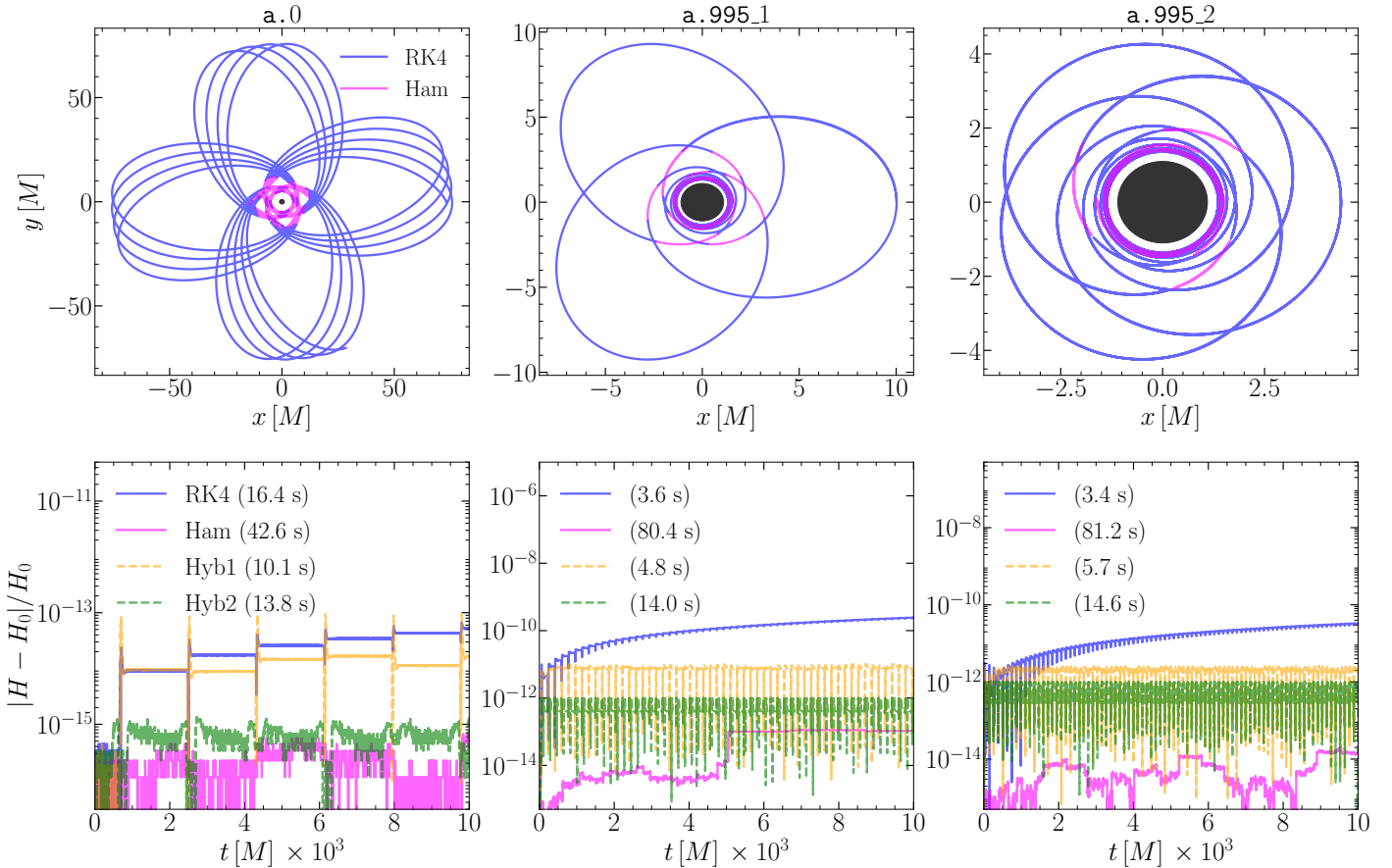


Fig. 5: Same trajectories for neutral particles as reported in Fig. 4, computed using our hybrid approaches. Top row: particle trajectories colour-coded according to the integrator adopted for the “Hyb2” scheme (see text for details and Tab. C.2 for the numerical parameters). The RK4 integrator (blue) is employed when the particle is far from the black hole, while the Hamiltonian scheme (magenta) is primarily used as the particle enters stronger gravitational-field regions. Bottom row: energy violations obtained using fixed integrator schemes (solid lines) and our hybrid approaches (dashed lines). The total runtime, in seconds, is also reported for each case.

the *periastron*, and the energy error exhibits a sudden “jump” before returning to a constant level. This evolution - in a sort of Heaviside-like fashion - suggests that the RK4 scheme performs reasonably well for most of the simulation, except when the particle experiences stronger gravitational forces where a more accurate integrator is required. In light of this, we propose a hybrid scheme that can self-consistently switch between the RK4 and the Hamiltonian integrator.

The key idea behind the hybrid scheme is simple yet efficient: at each timestep n , we monitor the violation of the Hamiltonian $\tilde{H}^{n+1} := |H(t^{n+1}) - H_0|/H_0$ and select the most suitable integrator accordingly. We first update the particle positions and momenta with the RK4 method to obtain the Hamiltonian energy at timestep $n + 1$. If a prescribed condition is satisfied, the updated particle position and velocity are accepted, otherwise, the step is rejected and the Hamiltonian integrator is employed instead. We consider two alternative criteria for this condition: the first, constrains the time derivative $\partial_t \tilde{H}^{n+1} < (\partial_t \tilde{H})_{\max}$, while the second, directly constrains the value $\tilde{H}^{n+1} < \tilde{H}_{\max}$. We will refer to these two approaches as “Hyb1” and “Hyb2”, respectively (See Tab. C.2 for details on numerical parameters.)

In Fig. 5 we show the results for our hybrid approach, for the same trajectories shown in Fig. 4. In the first row we report the trajectory for each case, colour-coded according to the integrator employed when using the “Hyb2” scheme. Notice that

the RK4 scheme is fully employed when the particle’s trajectory is far from the black hole, while it switches to the Hamiltonian scheme as the particle approaches it. In the bottom row we present a comparison of the Hamiltonian violation for different integration schemes, according to the legend, where we also report the total runtime (in seconds), when fixing all the other numerical parameters. As a reference and for all the three cases, the energy violation for the RK4 and Hamiltonian schemes are reported with solid lines in blue and magenta, respectively. Two additional hybrid simulations are shown with dashed lines, taking advantage of the stability of the Hamiltonian integrator at larger timesteps and using adaptive timesteps, reporting results for “Hyb1” (orange lines), and “Hyb2” (green lines).

Interestingly, the hybrid approach is able to speed up the simulation while retaining a smaller error violation, for example, comparing “Hyb1” (orange line) and “RK4” (blue line) for the case a.0 in the left panels of Fig. 5. Alternatively, it is possible to achieve even smaller error violations at a slightly higher computational cost, as shown for the “Hyb2” case (green line). In this case, the ratio between computational cost and accuracy improves significantly, with relative errors remaining at the level of $\lesssim 10^{-15}$, and a substantial speedup compared to the RK4 scheme, as well as the Hamiltonian integrator (magenta line).

Similar strategies can also be applied to the spinning cases a.995_1 and a.995_2 (shown in the middle and right columns

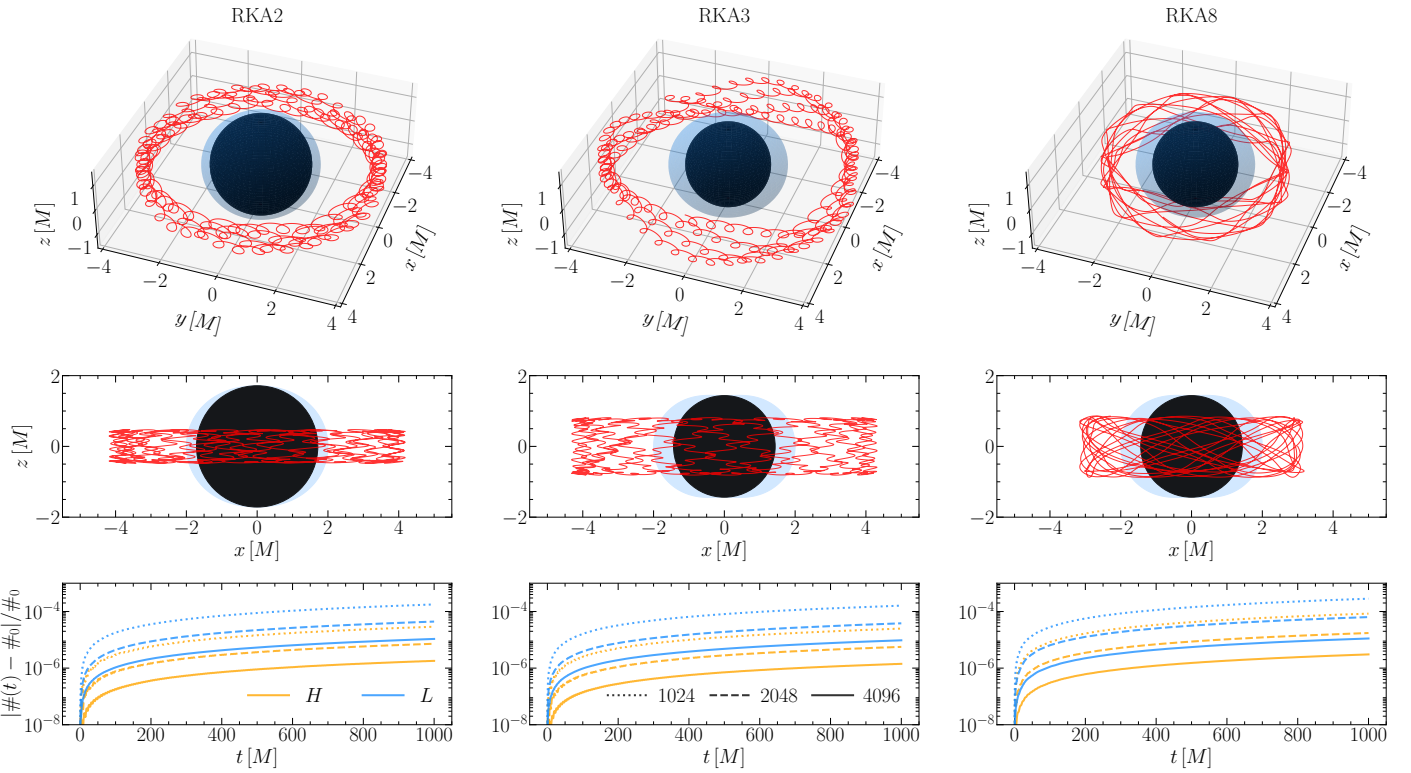


Fig. 6: Top: 3D charged particle trajectories around Kerr black holes, for different cases; Central: projection on the (x, z) plane, for the same trajectories; Bottom: conservation of H (yellow) and L (blue) for different spatial resolutions $N = N_r = N_\theta$, according to the legend. The horizon is reported as a black sphere, and the ergosphere as a blue shaded area. The physical and numerical parameters are reported in Tab. C.1.

of the same Figure). Here, the performance gain is reduced because the trajectory remains closer to the black hole compared to the Schwarzschild case, but the hybrid approaches still represent a valid compromise between speedup and accuracy.

3.1.3. Charged particles

Next step is to combine the effects of gravitational and electromagnetic fields which is essential for realistic PIC simulations. Following the approach of Bacchini et al. (2019); Chen et al. (2025), we evaluate the paths of charged particles embedded in a vacuum Wald field solution, with initial four-potential given by (Komissarov 2004):

$$A_\mu = \frac{B_0}{2} (g_{0\varphi} + 2a_* g_{00}, g_{r\varphi} + 2a_* g_{0r}, 0, g_{\varphi\varphi} + 2a_* g_{0\varphi}). \quad (44)$$

From the above expression, the \mathbf{E} and \mathbf{B} field can be obtained by:

$$B^i = \frac{1}{\sqrt{\gamma}} \eta^{ijk} \partial_j A_k, \quad (45)$$

$$E_i = -\partial_i A_0 - \partial_0 A_i, \quad (46)$$

and reported in detail in the Appendix B.1. Following the notation of Chen et al. (2025), we have selected the non-chaotic orbits labelled as RKA2, RKA3, and RKA8. Both the metrics are described by Kerr black holes, with dimensionless spin parameter $a_* = 0.7$ for RKA2, and $a_* = 0.9$ for RKA3 and RKA8. Even if the gravitational and electromagnetic fields are stationary and analytically known, here we aim to test the interpolation scheme in FPIC, as done in typical kinetic simulations. We start with $N_r = N_\theta = N = 1024$ collocation points,

with a radial domain covering $0.99 r_h \leq r \leq 6 M$ and a polar one $1/200 \leq \theta/\pi \leq 199/200$. For all the cases we use a fixed timestep $\Delta t = 10^{-3}$, and we set $q = m = 1$ for the particle's charge and mass. We use the RK4 scheme integrating the trajectories up to $t = 10^3 M$, which is greater than the typical timescales of GRPIC simulations.

A 3D visualization of the integrated charged trajectories is shown in the top row of Fig. 6 for the different cases, while in the central row we report a polar projection, in the (x, z) plane. Note that for each case, we report the horizon as a black central sphere, and the ergosphere as a light-blue shaded area. We also computed the energy conservation properties of the particle integrator in FPIC for charged particle trajectories, as the Hamiltonian H and the angular momentum L . In the presence of the electromagnetic field, the vector potential must be evaluated and added in the expression for the conserved energy, according to:

$$H = -u_0 - \frac{q}{m} A_0, \quad A_0 = B_0 \frac{a_* r (1 + \cos^2 \theta)}{r^2 + a_*^2 \cos^2 \theta}. \quad (47)$$

Similarly, the conserved angular momentum becomes:

$$L = u_\varphi + \frac{q}{m} A_\varphi, \quad A_\varphi = \frac{\sin^2 \theta}{2} \left[r^2 + a_*^2 - \frac{2a_*^2 r (1 + \cos^2 \theta)}{r^2 + a_*^2 \cos^2 \theta} \right]. \quad (48)$$

In the bottom row of Fig. 6 we report both the conservation of energy (yellow lines) and angular momentum (light-blue lines) for each case, when a spatial resolutions of $N = 1024, 2048$ and 4096 is used. The errors clearly decrease with increasing the number of mesh points, indicating that the conservation of H and L is essentially dominated by the interpolation of field

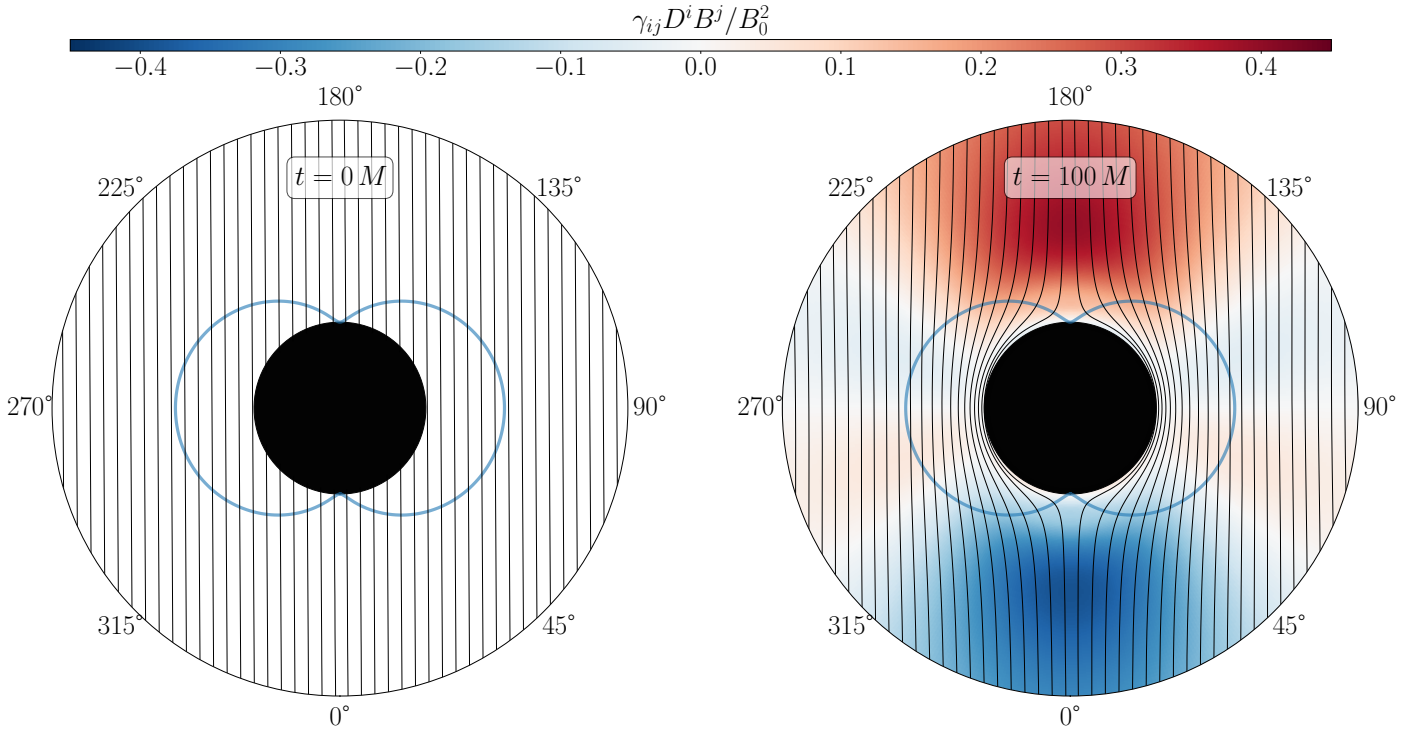


Fig. 7: Vacuum Wald solution for a rotating black hole with spin $a_* = 0.999$. Left: Initial state, which is the Wald solution for a non-rotating black hole; Right: Steady state at $t = 100 M$. The colormap report the parallel electric field $D_i B^i / B_0^2$. Black solid contours show magnetic-field lines (being the isocontours of the potential vector A_φ). The solid black sphere shows the horizon of the black hole and the light-blue curve shows the ergosphere. In the steady state (right panel), magnetic-field lines are expelled from the horizon.

values from the grid points to the particle positions. As a confirmation, we measured identical errors, when halving or doubling the timestep, with a fixed number of grid points, or when using the more demanding IMR scheme (not shown here). In light of this, we found the RK4 integrator to be the best compromise, as it is the least computationally demanding, and using a higher-order particle integrator provides limited benefit at a fixed spatial resolution. Finally, it is worth mentioning that typical values for large-scale GRPIC simulations are $N \gtrsim 1024 - 4196$, $\Delta t \lesssim 10^{-4} M$, and $t_{\text{final}} \sim 100 - 200 M$, making these errors adequate for our purposes.

3.2. Vacuum Wald Solution

To test the correctness of our Maxwell equation solver, we simulate a uniform magnetic field in electrovacuum. This choice is astrophysically motivated from currents located in a remote accretion disk naturally producing a large-scale magnetic field which is almost uniform at the black hole scale. The steady state solution assumes that the energy density of the field is small enough so that it does not significantly change the spacetime metric. In the case of an external field aligned with the spin axis of the black hole, the solution was found by [Wald \(1974\)](#), and was generalized to arbitrary inclinations by [Bicak & Janis \(1985\)](#).

We initialise the axisymmetric computational domain starting from within the event horizon, thus in a region causally disconnected from the rest of the domain, with a radial extent of $0.99 r_h \leq r \leq 20M$ and a polar one covering the full angle of $0 \leq \theta \leq 2\pi$, via $N_r \times N_\theta = 4196 \times 1024$ cells. An additional outer layer with absorbing boundary conditions for the electromagnetic fields is applied at $r = r_{\text{abs}} = 0.9 r_{\text{max}}$, according to

Eqs. (41) and (42). We immerse a rotating black hole with dimensionless spin parameter $a_* = 0.999$ into a uniform Wald-solution field with strength $B_0 = 10^3$. Even if the spacetime is described by a highly rotating Kerr metric, the initial Wald field is the solution for a Schwarzschild black hole (i.e., we set $a_* = 0$ in Eq. (44)), and let the system evolve. The electric field measured on the grid is initially $E_i = 0$, while the electric field measured by FIDOs is nonzero and reads $\mathbf{D} = -\boldsymbol{\beta} \times \mathbf{B}/\alpha$, according to Eq. (10). In the left panel of Fig. 7 we report the initial state of the simulation, with the parallel electric field $D_i B^i$ vanishing everywhere, while vertical lines represent the magnetic field.

Since the initial magnetic configuration is not solution for a spinning black hole, the field naturally evolve and establish a new steady state which agrees with the spinning Kerr metric, converging towards the Wald configuration. Right panel of Fig. 7 shows the steady state obtained at $t = 100 M$. The solution is characterized by the expulsion of the magnetic-field lines away from the horizon, phenomenon often called the *Meissner effect*. The parallel electric field $D_i B^i / B_0^2$ is no more vanishing as in the initial state, because the rotation of the black hole induces a strong unscreened electric field parallel to the magnetic field, as reported in the right panel of Fig. 7. The electric field is distributed according to a quadrupolar-like angular distribution, with maxima located around the polar regions and reaching values of the order of $D_i B^i \lesssim B_0$. The occurrence of gravitationally induced parallel electric fields $D_i B^i$ is another major feature of the Wald solution, and it is capable of accelerating particles and driving currents.

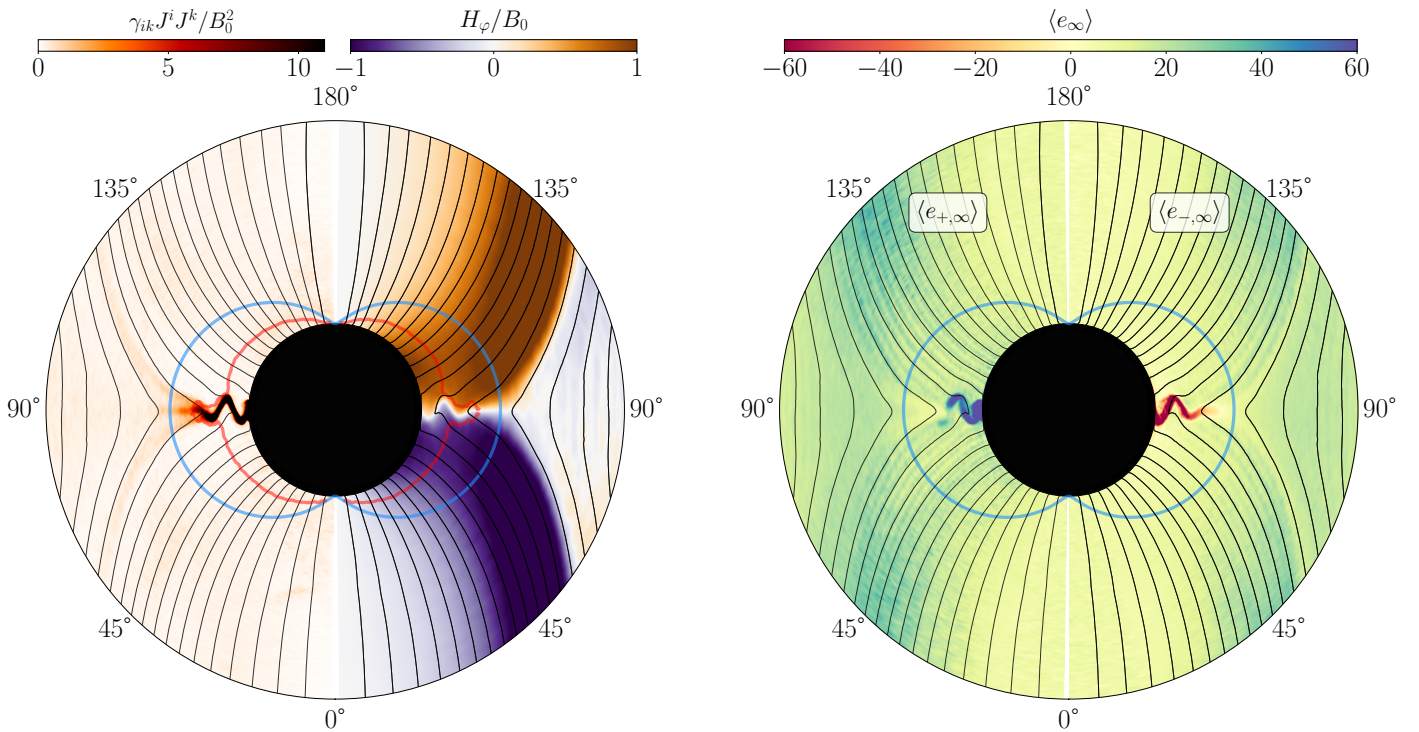


Fig. 8: Plasma-filled Wald solution for black hole spin $a_* = 0.999$, at $t = 40 M$. Left panel: square of the total current density J^2/B_0^2 (left), and toroidal magnetic field H_φ/B_0 (right). Shown in red there is the inner light surface, always located inside the ergosphere (reported with light-blue line). Right panel: averaged energy at infinity $e_\infty = -u_0$ for positrons (left) and electrons (right). Negative-energy electrons are present inside the current sheet.

3.3. Plasma-filled Wald Solution

The natural extension is to simulate a plasma-filled magnetosphere of a spinning black hole that is threaded by a uniform magnetic field (Parfrey et al. 2019; Chen et al. 2025). We initialise the electromagnetic fields with the exact Wald solution given by Eqs. (B.1)–(B.6), and setting $a_* = 0.999$. The computational domain covers a radial extent of $0.99 r_h \leq r \leq 20M$ and a polar one of $1/200 \leq \theta/\pi \leq 199/200$, via $N_r \times N_\theta = 4196 \times 1024$ cells. The magnetosphere is initially in electrovacuum, and we inject pair plasma into the spherical volume with coordinate radius $r_h \leq r \leq 6M$. In each computational cell, an electron-positron pair is added provided that $n < \mathcal{M}n_{\text{GJ}}$, where \mathcal{M} is the so-called ‘multiplicity’, $n = n_{e^-} + n_{e^+}$ is the total plasma density, n_{e^-}, n_{e^+} are the electron and positron number density, respectively, $n_{\text{GJ}} = -\boldsymbol{\Omega} \cdot \mathbf{B}/(4\pi e)$ is the Goldreich-Julian number density (Goldreich & Julian 1969), which measures the minimum number density required to screen the longitudinal components of the electric field, and $\boldsymbol{\Omega}$ is the angular velocity of the event horizon. We perform the injection of new particles every $\Delta t_{\text{inj}} = 0.01 M$ conferring an effective FIDO-measured density of $n_0 = 5 n_{\text{GJ}}$, and only for those cells for which the multiplicity condition $\mathcal{M} < 3$ is satisfied. We randomly draw the FIDO-frame particle velocities from a relativistic Maxwell-Jüttner of dimensionless temperature $\Theta := k_B T/m_e = 0.5$, with k_B being the Boltzmann constant.

The initial magnetic-field strength B_0 is specified in terms of the dimensionless field $\tilde{B}_0 := r_g/r_L = GM e B_0/(m_e c^4)$ where $r_g := GM/c^2$ is the gravitational radius, $r_L := m_e c^2/(e B_0)$ is the Larmor radius. Following Parfrey et al. (2019), we set $\tilde{B}_0 = 10^3$, which is equivalent to a magnetic field of $\simeq 1$ G for a black hole of mass $M \simeq 10 M_\odot$ (or of $\simeq 10^{-5}$ G for a black hole with

the mass of Sgr A*, i.e., $M \simeq 10^6 M_\odot$). With our choice of magnetic-field strength and spin, the ‘cold’ plasma magnetisation is $\sigma_0 = B_0^2/(4\pi n_{\text{GJ}} m_e) \simeq 2000$.

In contrast to the vacuum case where the magnetic-field lines were expelled out from the horizon, now the steady state is composed of a series of field lines threading the ergosphere, dragged and twisted by the rotation of space time, with a significant fraction passing through the black hole horizon. An equatorial current sheet quickly forms at the horizon, where the plasma falls along the field lines toward the black hole. At $t \sim 40 M$ the current sheet extends to the ergosphere boundary, being disrupted by the drift-kink instability (left panel of Fig. 8, left side, where we report J^2/B_0^2). When the steady state is reached, the toroidal magnetic field H_φ is large in the jet ($H_\varphi \sim B_0$), and very small outside it, as reported in the left panel of Fig. 8 (right side) for $t = 40 M$. Reported in light-blue is the ergosphere, and in red the inner light surface (always located inside the ergoregion), where the function $\mathcal{L}_{\text{ls}}(\Omega_f, r, \theta) := g_{\phi\phi} \Omega_f^2 + 2g_{t\phi} \Omega_f + g_{tt} = 0$ (Komissarov 2004), being $\Omega_f = -E_\theta/(\sqrt{\gamma} B^r)$ the angular velocity, and $g_{\mu\nu}$ is the background four-metric.

Rapidly rotating black holes naturally show the presence of particles with negative energy at infinity, i.e., $e_\infty := -u_0 < 0$, where u^μ is the particle’s four-velocity (Penrose 1969; Penna 2015; Hirotani et al. 2021; El Mellah et al. 2022)). Under these conditions, a Penrose process is possible, whereby energy can be extracted from a Kerr black hole when the negative-energy particles cross the event horizon (Penrose 1969). We report the cell-averaged energy at infinity $\langle e_\infty \rangle$ in the right panel of Fig. 8 for positrons (left) and electrons (right). Electrons with $\langle e_\infty \rangle < 0$ are ubiquitous in the current sheet, eventually falling toward the

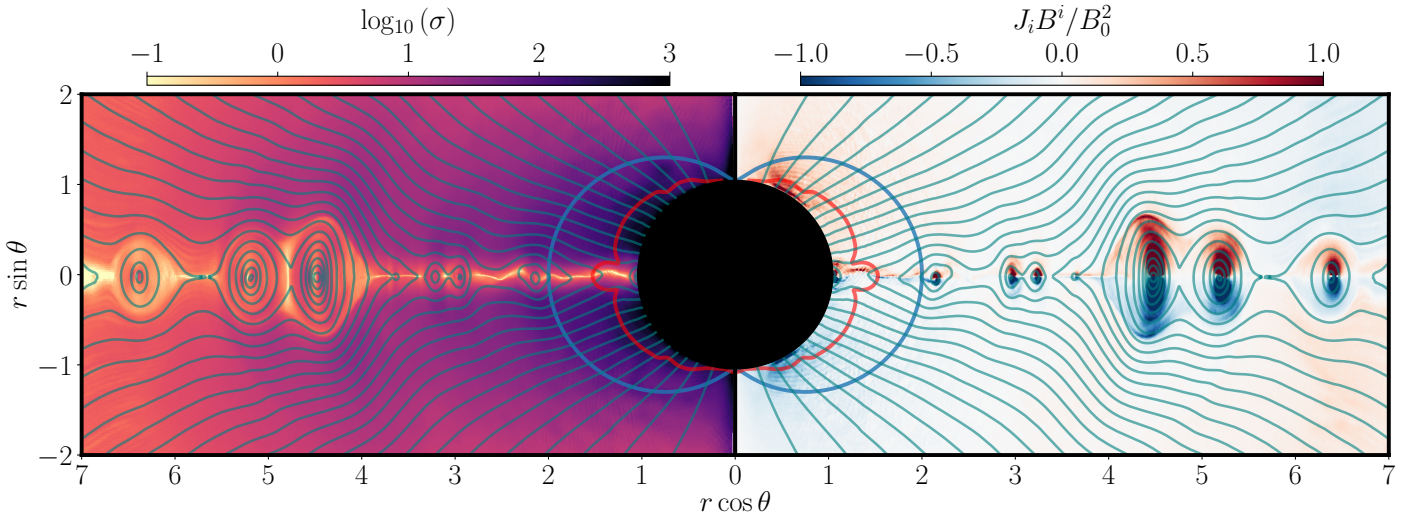


Fig. 9: Overview of a representative simulation with spin parameter $a_* = 0.999$, at time $\bar{t} = 14 M$. *Left panel*: “cold” plasma magnetisation $\sigma := \gamma_{ij} B^i B^j / (4\pi n m_e)$. *Right panel*: alignment between the current density and the magnetic field, $\gamma_{ij} J^i B^j / B_0^2$. Also shown are the ergosphere (light-blue), the inner light surfaces (red), and magnetic field lines (teal). The current sheet is located at the equatorial plane where magnetic reconnection takes place and a plasmoid-chain forms. Note that two plasmoids are going to merge at $r \sim 5 M$.

horizon and extracting rotational energy, according to the Penrose process.

3.4. The Split Monopole

For the split monopole case we initialise the radial component of the FIDO magnetic field as $B^r := \partial_\theta \Psi / \sqrt{\gamma}$, where $\Psi(r, \theta)$ is the gauge-invariant magnetic-flux function $\Psi(r, \theta) = 4M^2 B_0 \zeta(\theta)(1 - \cos \theta)$ (see the Appendix B.2 for details). The factor $\zeta(\theta)$ is introduced to model the equatorial current-sheet necessary to sustain the field discontinuity (Gralla & Jacobson 2014; Meringolo et al. 2025). In the presence of spacetime rotation, the initial split-monopole evolves towards a stationary electrovacuum configuration that preserves a monopolar topology in the polar plane and an equatorial current-sheet, while exhibiting gravitationally-induced toroidal magnetic fields, as well as electric fields along the magnetic-field lines. These gravitationally induced electromagnetic fields are similar to what observed in the Wald solution (Wald 1974) as considered, for instance, in Mösta et al. (2010); Alic et al. (2012); Parfrey et al. (2019).

After the vacuum electromagnetic fields settle to a stationary configuration at $t = t_{\text{inj}} = 50 M$, a e^-/e^+ -pair plasma is injected in the spherical volume with coordinate radius $r_h < r < 15 M$. In each computational cell, an electron-positron pair is added for all subsequent times $\bar{t} := t - t_{\text{inj}} > 0$, provided that the condition $n < \mathcal{M} n_{\text{GJ}}$ is satisfied, and we set the multiplicity to $\mathcal{M} = 10$ so as to have an accurate representation of the black hole magnetosphere. We have verified that, in this way, the magnetosphere in our simulations obeys $\sigma := B_i B^i / (4\pi n m_e) \gg \Gamma$ (Beskin 1997), with typical values of $\sigma \gtrsim 100$ and $\sigma/\Gamma \gtrsim 10$.

We carried out an extensive campaign of GRPIC simulations, varying the dimensionless spin parameter a_* while keeping all other parameters fixed (details and results are reported in Meringolo et al. (2025)). In Fig. 9 (left panel), we report a representative view of the black hole magnetosphere for the most extreme configuration considered, namely a Kerr black hole with spin $a_* = 0.999$. The left panel shows the magnetisation σ at

$\bar{t}/M = 14$, when the simulation has reached a stationary state and a chain of plasmoids has fully formed. A current sheet is clearly visible along the equatorial plane, where magnetic reconnection occurs and $\sigma \lesssim 1$ due to the high plasma density along the layer. Plasmoid formation is ubiquitous along the current sheet: two large magnetic structures are visible at $r \sim 5 M$, moving away from the black hole and merging to form a larger plasmoid.

In the right panel, we instead show the alignment between the current density and the magnetic field, $\gamma_{ij} J^i B^j / B_0^2$. As expected, a strong alignment is present inside the closed field lines of the plasmoids, with a polarity reversal across the equatorial plane. We overplot magnetic-field lines (teal), highlighting that the split-monopole configuration is strongly perturbed by plasmoid formation and dynamics. Also shown in Fig. 9 is the region inside the outer event horizon r_+ (black-shaded area) and the position of the ergosphere, or static limit, (light-blue line). Within the inner light surface (shown with red line), massive particles cannot corotate and acquire instead large radial infalling velocities at all latitudes, reaching Lorentz factors up to $\Gamma \sim 200$ and comparable to those observed for the particles accelerated by the magnetic reconnection along the equatorial plane.

Using our large set of simulations, we have been able to measure the power associated with the Blandford-Znajek (BZ) mechanism, which provides an efficient conversion of black-hole rotational energy into electromagnetic energy and operates in force-free black-hole magnetospheres (Blandford & Znajek 1977). We compute the power extracted via the BZ mechanism by evaluating the Poynting flux through a two-sphere located close to the event horizon, according to

$$P_{\text{BZ}} = \int (T^r)_{\text{EM}} \sqrt{-g} d\theta d\phi = 2\pi \int_0^\pi S^r \sqrt{\gamma} d\theta, \quad (49)$$

where \mathbf{T}_{EM} is the electromagnetic part of the energy-momentum tensor, and $S^r := (E_\theta H_\phi - E_\phi H_\theta) / (4\pi \sqrt{\gamma})$ is the radial component of the Poynting vector. The (time-averaged) results of our GRPIC simulations are reported with black filled circles in the right panel of Fig. 10, with the corresponding error-bars. Notice that we normalise the powers to $P_{\text{BZ0}}^{\text{max}} \approx 10^{-3} (\Phi_h/M)^2$, represent-

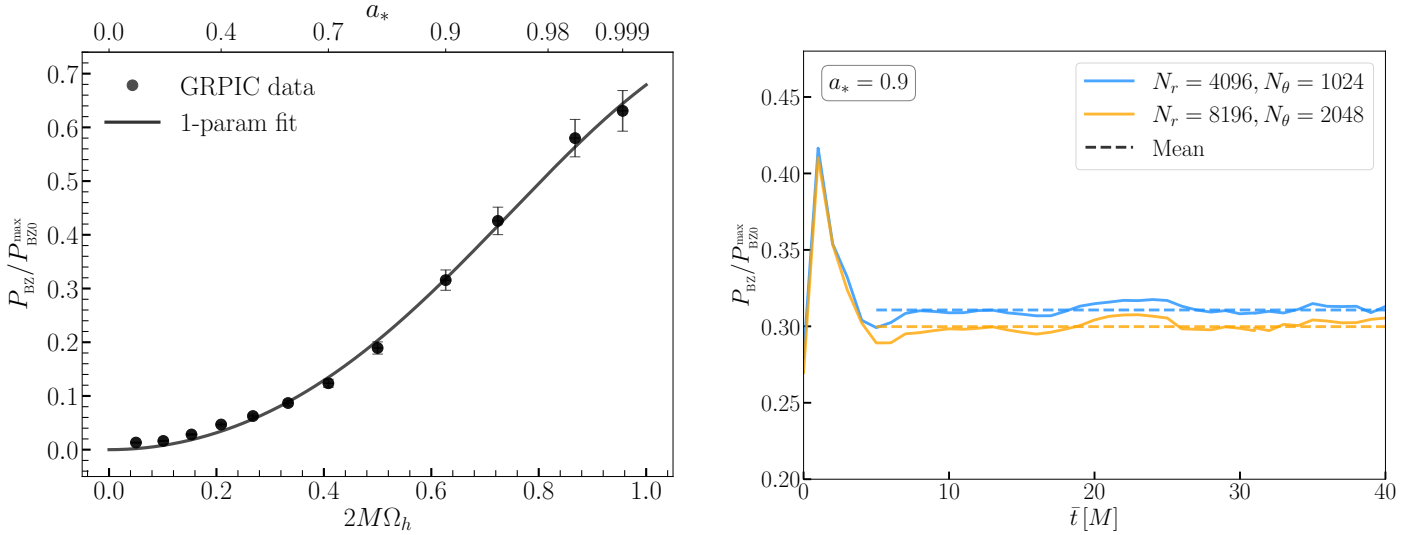


Fig. 10: *Left panel*: Normalized BZ luminosity, as a function of the black-hole angular velocity (see the top horizontal axis for a mapping in terms of the dimensionless spin of the black hole) for all of our GRPIC simulations (black filled circles) and with the associated numerical errors. The black solid line shows the analytic expression (Equation (51)) after rescaling the factor κ to account for the specific magnetic-field topology (one-parameter fit). *Right panel*: Resolution test for the representative spin $a_* = 0.9$, showing the time evolution of the normalized power. The number of points N_r and N_θ are reported in the legend for each case, while dashed lines report the respective averages, computed in the time window $5 \leq \bar{t}/M \leq 40$.

ing the maximum value of the original BZ estimate attained for $M\Omega_h = 1/2$, and where Φ_h is the (half-hemisphere) magnetic flux (Meringolo et al. 2025). Expression (49) can be modelled generically as

$$P_{BZ} = \frac{\kappa}{4\pi} \Phi_h^2 F(\Omega_h), \quad (50)$$

being κ a scaling factor related to the topology of the magnetosphere only, and $F(\Omega_h)$ a function of the spin of the black hole. Recently, using analytic techniques that combine perturbation theory with a matched-asymptotic expansion scheme (Armas et al. 2020; Camilloni et al. 2022), it was possible to obtain high-order corrections in $F(\Omega_h)$ up to $O(\Omega_h^8)$, namely

$$F_{\text{an}}(\Omega_h) = \Omega_h^2 \left[1 + \tilde{\alpha}(M\Omega_h)^2 + \tilde{\beta}(M\Omega_h)^4 + \tilde{\gamma}|M\Omega_h|^5 \right. \\ \left. + (\tilde{\delta} + \tilde{\epsilon} \log |M\Omega_h|)(M\Omega_h)^6 \right] + O(M^9 \Omega_h^9). \quad (51)$$

The black solid line in Fig. 10 reports the expression (50), combined with the dependence (51), where a one-parameter fit was made to fix the scaling factor $\kappa = 0.041$.

In the right panel of Fig. 10, we show the time evolution of P_{BZ}/P_{BZ0}^{\max} for a representative simulation with $a_* = 0.9$, while varying the grid resolution and keeping all other parameters fixed. The light-blue line represents the standard resolution we used in all our split-monopole campaign of simulations, whereas the orange line shows the result of a simulation with twice the number of grid points in both the r - and θ -direction. We note that a peak in the BZ power suddenly appears when the first particle injection starts at $\bar{t}/M = 0$, perturbing the stationary electrovacuum configuration. To avoid unphysical measurements, we compute the averaged power only after stationarity is reached, by taking the mean value of P_{BZ}/P_{BZ0}^{\max} in the time interval $5 \leq \bar{t}/M \leq 40$. The dashed lines (with the corresponding colour code) indicate the mean values for the two resolutions, which correspond to normalized powers of 0.316 and 0.299, respectively, with a relative difference of $\lesssim 6\%$.

4. Conclusions

We have presented FPIC, a newly developed PIC code for the solution of collisionless plasma in curved spacetimes and in the vicinity of black holes. With the goal of ensuring the reproducibility of the results obtained with FPIC, we have provided a detailed discussion of the numerical methods employed to solve the equations of motion of the particles and the evolution equations for the electromagnetic fields.

While most of the methods employed are well-known and have been used in other numerical codes of this type, we have also proposed a new hybrid approach for the evolution of the equations of motion of the charged particles. In the novel method, the time integrator is not kept fixed but chosen in real time based on the evolution of the energy error, which is monitored either via its time derivative or via its instantaneous value. The key idea is simple yet effective: far from the black hole, the robust and efficient RK4 integrator ensures a good energy conservation, but loses precision as the particle nears the black-hole event horizon. In such regions, a more accurate scheme – such as the Hamiltonian integrator – would be preferable, but its computational costs are considerably higher. An optimal compromise can be obtained by switching between the two methods on the basis of the degree of curvature of the spacetime. Furthermore, by taking advantage of the stability of the Hamiltonian integrator at larger timesteps, an adaptive timestep is employed when switching between the two schemes. The result of this approach is a particle pusher that guarantees high precision at comparatively small computational costs.

The numerical methods described in this way were then applied to a number of testbeds aimed at validating the correctness of the code, testing its robustness, and assessing its performance. The tests carried out concentrated on the evolution of particles (neutral and charged) near black holes, on the evolution of the electromagnetic fields in vacuum, and on the combination of the two in genuine PIC simulations. More specifically, within the first class of tests, we have considered the dynamics of a neu-

tral particle in the Schwarzschild and Kerr metrics, as well as that of a charged particle embedded in a background Wald magnetic field, in rotating black-hole spacetimes with different spins. Besides reproducing well-known behaviours of the particles under the influence of gravity and of a Lorentz force, the use of the hybrid approach provides high precision with errors being dominated by the interpolation scheme used to couple fields and particles. For the second class of test, on the other hand, we have validated the code’s ability to recover the vacuum Wald solution for a rotating black hole when initialised with the Schwarzschild Wald solution. In this case, a so-called Meissner effect expels out the magnetic-field lines threading the horizon, reaching a stationary regime.

Finally, we have tested the robustness of code with fully GR-PIC scenarios in which a pair plasma is evolved self-consistently with the electromagnetic fields that are produced by its dynamics. In the case in which the electrovacuum Wald solution is filled with a pair plasma, we observed that the magnetic-field lines threading the ergosphere are dragged into the black hole and form an equatorial current sheet within the ergosphere. Electrons with negative energy at infinity are ubiquitous inside the ergosphere along the current sheet, indicating that the Penrose process is active there. In addition, we have presented results for a rotating black hole threaded by a split-monopole magnetic field. This configuration is well-known to generate a current sheet near the equatorial plane and to trigger magnetic reconnection, which is responsible for the production of chains of relativistic plasmoids (see [Meringolo et al. 2025](#), for details). For these calculations we have measured the power associated with the Blandford and Znajek mechanism, finding excellent agreement with the high-order predictions coming from perturbation theory. Because the match requires the calculation of a single coefficient independent of the black-hole spin and related to the specific magnetic-field topology, the excellent match is a very strong validation test.

In summary, we have presented in detail the numerical methods to be implemented in the construction of a PIC code within a general-relativistic framework and shown that a code built in this way, i.e., FPIC is to reproduce correctly and accurately fully nonlinear plasma dynamics near rotating black holes. While a number of applications await the use of this code, a number of extensions are possible. First, we recall that we have adopted a simplified pair-plasma injection scheme based on the local Goldreich-Julian density. We found that this approach substantially speeds up the simulations while yielding results that are both qualitatively and quantitatively consistent with those obtained using more sophisticated and physically detailed injection prescriptions ([Parfrey et al. 2019](#); [El Mellah et al. 2022](#); [Chen et al. 2025](#)). Nonetheless, to achieve fully realistic magnetospheric modelling, more accurate particle-injection strategies need to be developed and tested. Second, as customary in PIC simulations, our approach ignores radiative processes, which may however play a role under specific physical conditions and, in particular, when the particle experience extremely large accelerations near the black-hole horizon. Hence, future developments will have to focus on implementing inverse-Compton emission, photon-photon pair-production mechanisms, and radiation-reaction forces. Finally, but not less importantly, to model ever more realistic astrophysical scenarios, the code testing and validation needs to be extended to fully 3D configurations. Because the associated computational costs easily become unsustainable when the calculations are performed with CPUs, FPIC need to be extended with a hybrid MPI-OpenMP parallelisation strategy that includes GPU acceleration through OpenMP

offloading. Progress in many of these directions is already ongoing and will be presented in future works.

Acknowledgements. It is a pleasure to acknowledge Björn Dick, Tobias Haas, Markus Kurz, Hirav Patel, and Johanna Potyka, for their help and the fruitful discussion at the hackathon *Porting and Optimization for Hunter* at HLRS, Stuttgart, Germany. We are also grateful to F. Camilloni for useful discussions and suggestions. This research was supported by the ERC Advanced Grant JET-SET: Launching, propagation and emission of relativistic jets from binary mergers and across mass scales (Grant No. 884631). L.R. acknowledges the Walter Greiner Gesellschaft zur Förderung der physikalischen Grundlagenforschung e.V. through the Carl W. Fueck Laureatus Chair. The simulations were performed on HPE Apollo HAWK at the High Performance Computing Center Stuttgart (HLRS) under the grant BNSMIC, on SuperMUC-NG at the Leibniz Supercomputing Centre (LRZ) under the grant MICMAC, and on the local ITP Supercomputing Clusters Goethe-HLR, Iboga and Calea.

References

Alic, D., Moesta, P., Rezzolla, L., Zanotti, O., & Jaramillo, J. L. 2012, *Astrophys. J.*, 754, 36
 Armas, J., Cai, Y., Compère, G., Garfinkle, D., & Gralla, S. E. 2020, *JCAP*, 04, 009
 Asenjo, F. A. & Comisso, L. 2017, *Phys. Rev. Lett.*, 118, 055101
 Bacchini, F., Ripperda, B., Chen, A. Y., & Sironi, L. 2018, *Astrophys. J., Supp.*, 237, 6
 Bacchini, F., Ripperda, B., Porth, O., & Sironi, L. 2019, *Astrophys. J., Supp.*, 240, 40
 Baumgarte, T. W. & Shapiro, S. L. 2010, *Numerical Relativity: Solving Einstein’s Equations on the Computer* (Cambridge, UK: Cambridge University Press)
 Beskin, V. S. 1997, *Soviet Physics Uspekhi*, 40, 659
 Bicak, J. & Janis, V. 1985, *Mon. Not. R. Astron. Soc.*, 212, 899
 Birdsall, C. K. & Langdon, A. B. 2005, *Plasma Physics via Computer Simulation (Reprinted)*
 Blandford, R. D. & Znajek, R. L. 1977, *Mon. Not. R. Astron. Soc.*, 179, 433
 Bransgrove, A., Ripperda, B., & Philippov, A. 2021, *Phys. Rev. Lett.*, 127, 055101
 Camilloni, F., Dias, O. J. C., Grignani, G., et al. 2022, *Journal of Cosmology and Astroparticle Physics*, 2022, 58
 Camilloni, F., Harmark, T., Orselli, M., & Rodriguez, M. J. 2024, *Journal of Cosmology and Astroparticle Physics*, 2024, 047
 Camilloni, F. & Rezzolla, L. 2025, *Astrophys. J. Lett.*, 982, 10
 Cerutti, B., Philippov, A., Parfrey, K., & Spitkovsky, A. 2015, *Mon. Not. R. Astron. Soc.*, 448, 606
 Chen, A. Y., Luepker, M., & Yuan, Y. 2025, *arXiv e-prints*, arXiv:2503.04558
 Comisso, L. & Asenjo, F. A. 2021, *Phys. Rev. D*, 103, 023014
 Crinquand, B. 2021, *Theses, Université Grenoble Alpes [2020-....]*
 Crinquand, B., Cerutti, B., Dubus, G., Parfrey, K., & Philippov, A. 2021, *Astron. Astrophys.*, 650, A163
 Crinquand, B., Cerutti, B., Dubus, G., Parfrey, K., & Philippov, A. 2022, *Phys. Rev. Lett.*, 129, 205101
 Crinquand, B., Cerutti, B., Philippov, A., Parfrey, K., & Dubus, G. 2020, *Phys. Rev. Lett.*, 124, 145101
 Cruz-Ororio, A., Fromm, C. M., Mizuno, Y., et al. 2022, *Nature Astronomy*, 6, 103
 Cruz-Ororio, A., Meringolo, C., Fromm, C. M., et al. 2025, *arXiv e-prints*, arXiv:2512.14835
 Das, P., Porth, O., & Watts, A. L. 2022, *Monthly Notices of the Royal Astronomical Society*, 515, 3144
 Del Zanna, L., Tomei, N., Bugli, M., & Bucciantini, N. 2020, in *Journal of Physics Conference Series*, Vol. 1623, *Journal of Physics Conference Series*, 012004
 Dhruv, V., Prather, B., Wong, G. N., & Gammie, C. F. 2025, *Astrophys. J., Supp.*, 277, 16
 Dihingia, I. K., Mizuno, Y., Fromm, C. M., & Rezzolla, L. 2022, *arXiv e-prints*, arXiv:2206.13184
 El Mellah, I., Cerutti, B., & Crinquand, B. 2023, *Astron. Astrophys.*, 677, A67
 El Mellah, I., Cerutti, B., Crinquand, B., & Parfrey, K. 2022, *Astron. Astrophys.*, 663, A169
 Event Horizon Telescope Collaboration, Akiyama, K., Alberdi, A., et al. 2022, *Astrophys. J. Lett.*, 930, L12
 Event Horizon Telescope Collaboration, Akiyama, K., Alberdi, A., et al. 2019, *Astrophys. J. Lett.*, 875, L1
 Feng, K. 1986, *Journal of Computational mathematics*, 4, 279
 Figueiredo, E., Cerutti, B., & Parfrey, K. 2025, *Astron. Astrophys.*, 700, L19
 Fujibayashi, S., Shibata, M., Wanajo, S., et al. 2020, *Phys. Rev. D*, 101, 083029

Galishnikova, A., Hakobyan, H., Philippov, A., & Crinquand, B. 2025, arXiv e-prints, arXiv:2511.17701

Galishnikova, A., Philippov, A., Quataert, E., et al. 2023, Phys. Rev. Lett., 130, 115201

Goldreich, P. & Julian, W. H. 1969, *Astrophys. J.*, 157, 869

Gorard, J., Juno, J., & Hakim, A. 2025, arXiv e-prints, arXiv:2510.26019

Gralla, S. E. & Jacobson, T. 2014, *Mon. Not. Roy. Astron. Soc.*, 445, 2500

Hairer, E., Lubich, C., & Wanner, G. 2002, Geometric numerical integration.

Structure-preserving algorithms for ordinary differential equations, 2nd edn. (Springer)

Hirotani, K., Krasnopol'sky, R., Shang, H., Nishikawa, K.-i., & Watson, M. 2021, *Astrophys. J.*, 908, 88

Imbrogno, M., Meringolo, C., Cruz-Osorio, A., et al. 2025, *Astrophys. J. Lett.*, 990, L33

Imbrogno, M., Meringolo, C., Servidio, S., et al. 2024, *Astrophys. J. Lett.*, 972, L5

Iserles, A. 1986, *IMA Journal of Numerical Analysis*, 6, 381

Kerr, R. P. 1963, *Phys. Rev. Lett.*, 11, 237

Koide, S. & Arai, K. 2008, *Astrophys. J.*, 682, 1124

Komissarov, S. S. 2004, *Mon. Not. R. Astron. Soc.*, 350, 427

Levin, J. & Perez-Giz, G. 2008, *Phys. Rev. D*, 77, 103005

Levinson, A. & Cerutti, B. 2018, *Astron. Astrophys.*, 616, A184

Luepker, M., Yuan, Y., & Chen, A. Y. 2026, *Astrophys. J.*, 996, 75

McKinney, J. C., Tchekhovskoy, A., & Blandford, R. D. 2012, *Mon. Not. R. Astron. Soc.*, 423, 3083

Megale, R., Cruz-Osorio, A., Ficarra, G., et al. 2025, *Mon. Not. R. Astron. Soc.*, 544, 2011

Meringolo, C., Camilloni, F., & Rezzolla, L. 2025, *Astrophys. J. Lett.*, 992, L8

Meringolo, C., Cruz-Osorio, A., Rezzolla, L., & Servidio, S. 2023, *Astrophys. J.*, 944, 122

Mizuno, Y. & Rezzolla, L. 2024, arXiv e-prints, arXiv:2404.13824

Most, E. R., Noronha, J., & Philippov, A. A. 2022, *Monthly Notices of the Royal Astronomical Society*, 514, 4989

Mösta, P., Palenzuela, C., Rezzolla, L., et al. 2010, *Phys. Rev. D*, 81, 064017

Nathanail, A., Dhang, P., & Fromm, C. M. 2022, *Mon. Not. R. Astron. Soc.*, 513, 5204

Niv, I., Bromberg, O., Levinson, A., Cerutti, B., & Crinquand, B. 2023, *Mon. Not. R. Astron. Soc.*, 526, 2709

Parfrey, K., Philippov, A., & Cerutti, B. 2019, *Phys. Rev. Lett.*, 122, 035101

Penna, R. F. 2015, *Phys. Rev. D*, 91, 084044

Penrose, R. 1969, *Riv. Nuovo Cimento*, 1, 252

Pierre Jacques, T., Cupp, S., Werneck, L. R., et al. 2025, 0, 112, 084044

Press, W., Teukolsky, S., Vetterling, W., & Flannery, B. 1992

Rezzolla, L. & Zanotti, O. 2013, *Relativistic Hydrodynamics* (Oxford University Press)

Sironi, L., Rowan, M. E., & Narayan, R. 2021, *Astrophys. J. Lett.*, 907, L44

Sironi, L. & Spitkovsky, A. 2014, *Astrophys. J.*, 783, L21

Tanabe, K. & Nagataki, S. 2008, *Phys. Rev. D*, 78, 024004

Tchekhovskoy, A., Narayan, R., & McKinney, J. C. 2011, *Mon. Not. R. Astron. Soc.*, 418, L79

Thorne, K. S. & Macdonald, D. 1982, *Mon. Not. R. Astr. Soc.*, 198, 339

Torres, R., Grismayer, T., Cruz, F., Fonseca, R. A., & Silva, L. O. 2024, *New Astronomy*, 112, 102261

Tu, C. Y. & Marsch, E. 1997, *Solar Physics*, 171, 363

Uniyal, A., Dihingia, I. K., Mizuno, Y., & Rezzolla, L. 2025, *Nature Astron.*, 1, 8

van der Holst, B., Manchester, W. B., I., Frazin, R. A., et al. 2010, *Astrophys. J.*, 725, 1373

Vos, J., Cerutti, B., Mościbrodzka, M., & Parfrey, K. 2025, *Phys. Rev. Lett.*, 135, 015201

Wald, R. M. 1974, *Phys. Rev. D*, 10, 1680

Werner, G. R., Uzdensky, D. A., Begelman, M. C., Cerutti, B., & Nalewajko, K. 2018, *Mon. Not. R. Astron. Soc.*, 473, 4840

Wong, K., Zhdankin, V., Uzdensky, D. A., Werner, G. R., & Begelman, M. C. 2020, *Astrophys. J. Lett.*, 893, L7

Yee, K. 1966, *IEEE Transactions on Antennas and Propagation*, 14, 302

Yuan, Y., Chen, A. Y., & Luepker, M. 2025, *Astrophys. J.*, 985, 159

Zhdankin, V., Uzdensky, D. A., Werner, G. R., & Begelman, M. C. 2019, *Physical review letters*, 122, 055101

Appendix A: The Kerr metric

The spacetime around a stationary rotating black hole is described by the Kerr metric (Kerr 1963). In Kerr-Schild coordinates, the metric is given by (Komissarov 2004)

$$\gamma_{ij} = \begin{pmatrix} \xi & 0 & -a_*^2 \xi \sin^2 \theta \\ 0 & \rho^2 & 0 \\ -a_*^2 \xi \sin^2 \theta & 0 & \sin^2 \theta [\rho^2 + a_*^2 \xi \sin^2 \theta] \end{pmatrix}, \quad (\text{A.1})$$

$$\gamma^{ij} = \begin{pmatrix} \frac{a_*^2 \sin^2 \theta}{\rho^2} + \xi^{-1} & 0 & \frac{a_*}{\rho^2} \\ 0 & \frac{1}{\rho^2} & 0 \\ \frac{a_*}{\rho^2} & 0 & \frac{1}{\rho^2 \sin^2 \theta} \end{pmatrix}, \quad (\text{A.2})$$

where $\xi = 1 + 2Mr/\rho^2$ and $\rho^2 = r^2 + a_*^2 \cos^2 \theta$. The lapse function α and the shift vector $\beta^i = \beta^r$ read

$$\alpha = \xi^{-1/2}, \quad \beta^r = \frac{2Mr}{\rho^2 \xi} = \frac{\xi - 1}{\xi}, \quad (\text{A.3})$$

meaning that the grid is moving towards the black hole. This motion of the grid removes the well-known coordinate singularity at the event horizon present in the more widely used Boyer-Lindquist coordinates, but comes at the cost of a non-diagonal form of the spatial metric. The metric determinant is represented by

$$\gamma = \rho^4 \xi \sin^2 \theta. \quad (\text{A.4})$$

Note that the limit $a_* \rightarrow 0$ the above Kerr metric becomes diagonal and it reduces to the Schwarzschild metric.

10 Appendix B: Analytical initial conditions

B.1. The Wald solution

The stationary Wald field solution in the presence of a spinning black hole and consistent with a uniform magnetic field of strength \tilde{B}_0 in Kerr-Schild coordinates is given by

$$B^r = \frac{\tilde{B}_0}{\sqrt{\gamma}} \left[r^2 + a_*^2 - 2r + \frac{2r(r^4 - a_*^4)}{\rho^4} \right] \sin \theta \cos \theta, \quad (\text{B.1})$$

$$B^\theta = -\frac{\tilde{B}_0}{\sqrt{\gamma}} \left[r + a_*^2(1 + \cos^2 \theta) \frac{2r^2 - \rho^2}{\rho^4} \right] \sin^2 \theta, \quad (\text{B.2})$$

$$B^\varphi = -\frac{\tilde{B}_0}{\sqrt{\gamma}} \left[\frac{2a_*r(a_*^2 - r^2)}{\rho^4} - a_* \right] \sin \theta \cos \theta, \quad (\text{B.3})$$

$$E_r = \tilde{B}_0 a_* (1 + \cos^2 \theta) \frac{a_*^2 \cos^2 \theta - r^2}{\rho^4}, \quad (\text{B.4})$$

$$E_\theta = \tilde{B}_0 a_* \frac{2a_*r(a_*^2 - r^2)}{\rho^4} \sin \theta \cos \theta, \quad (\text{B.5})$$

$$E_\varphi = 0, \quad (\text{B.6})$$

where $\tilde{B}_0 = 10^3$ and the four-potential is reported in Eq. (44). From the covariant components of the electric field E_i , one can obtain the FIDO's electric field D_i by means of the relation (10), obtaining the contravariant components as $D^j = \gamma^{ij} D_i$. We have adopted the above set of equations (B.1)–(B.6) as initial conditions for the B^i and D^i fields in different cases: 1) in Section 3.1, when evolving the charged particles embedded in a magnetic field; 2) in Section 3.2, for the vacuum Wald test by setting $a_* = 0$ for the Schwarzschild solution; 3) in Section 3.3, for the plasma-filled Wald case.

B.2. The split-monopole solution

20 For the split monopole configuration presented in Section 3.4, we start from an electrovacuum solution in the Schwarzschild space-time, initialised by means of a magnetic-flux function $\Psi(r, \theta) = 4M^2 B_0 \zeta(\theta)(1 - \cos \theta)$. This standard split-construction is realised through a step-function ζ that introduces a current-sheet in the equatorial plane necessary to sustain the reversed polarity of the magnetic field (Gralla & Jacobson 2014). In our simulations we considered an approximate expression $\zeta = 2/\pi \arctan[\zeta_0(\theta - \pi/2)]$. After

the injection, once the magnetosphere settles in plasma-filled conditions, the simulation approaches solutions obtained from perturbative studies of FFE in Kerr spacetime (Blandford & Znajek 1977; Tanabe & Nagataki 2008; Armas et al. 2020; Camilloni et al. 2024), namely

$$B^r = -2\tilde{B}_0 \arctan\left[\frac{1}{2}\zeta_0(\pi - 2\theta)\right] \frac{1}{\pi\sqrt{r^3(2+r)}}, \quad (\text{B.7})$$

$$B^\theta = 0, \quad (\text{B.8})$$

$$B^\varphi = -\tilde{B}_0 \arctan\left[\zeta_0\left(-\frac{\pi}{2} + \theta\right)\right] \frac{a_*(4+r)}{4\pi\sqrt{r^5(2+r)}}, \quad (\text{B.9})$$

$$D^r = \tilde{B}_0 \arctan\left[\frac{1}{2}\zeta_0(\pi - 2\theta)\right] \frac{8+r(4+r)}{4\pi\sqrt{r^7(2+r)}} a_* \sin\theta, \quad (\text{B.10})$$

$$D^\theta = 0, \quad (\text{B.11})$$

$$D^\varphi = 0, \quad (\text{B.12})$$

$$J^r = \tilde{B}_0 \left\{ \arctan\left[\frac{1}{2}\zeta_0(\pi - 2\theta)\right] \cos\theta - \frac{2\zeta_0 \sin\theta}{4 + \zeta_0^2(\pi - 2\theta)^2} \right\} \frac{a_*}{2\pi r^2}, \quad (\text{B.13})$$

$$J^\theta = 0, \quad (\text{B.14})$$

$$J^\varphi = -\tilde{B}_0 \frac{8\zeta_0}{\pi(4 + \zeta_0^2(\pi - 2\theta)^2)r^4 \sin\theta}. \quad (\text{B.15})$$

In our split monopole configuration we used Eqs. (B.7)–(B.15) by setting $\tilde{B}_0 = 10^3$, $\zeta_0 = 10^3$ and $a_* = 0$.

Appendix C: Particle trajectories parameters

Here we report physical and numerical parameters for the test particle trajectories presented in Section 3.1. We split the data in Tab. C.1 in neutral-particle trajectories (top) and charged-particle trajectories (bottom). For the charged particles we used the same naming conventions and values reported in the literature (Levinson & Cerutti 2018; Bacchini et al. 2019; Chen et al. 2025). We also report in the Tab. C.2 the numerical parameters used in our hybrid approach for neutral particles, presented in the Subsection 3.1.2.

Table C.1: Initial conditions and parameters for particle trajectories reported in Subsections 3.1.1 (neutral particles, top rows) and 3.1.3 (charged particles, bottom rows). Starting from the left, the columns represent: The name of simulation, the dimensionless spin a_* , the initial magnetic-field parameter B_0 , the orbit’s energy E and angular momentum L , the initial particle position \mathbf{r} and four-velocity \mathbf{u} . In all the cases we initialised $\varphi^0 = 0$.

Name	a_*	B_0	E	L	$\{r^0, \theta^0\}$	$\{u_r^0, u_\theta^0, u_\varphi^0\}$
Neutral particles						
a.0	0.0	0.0	0.987649	3.9	$\{73.239804, \pi/2\}$	$\{0.027724, 0.0, 3.9\}$
a.995_1	0.995	0.0	0.916235	2.0	$\{10.021533, \pi/2\}$	$\{0.201211, 0.0, 2.0\}$
a.995_2	0.995	0.0	0.841423	1.82	$\{4.376281, \pi/2\}$	$\{0.487625, 0.0, 1.82\}$
Charged particles						
RKA2	0.7	2.0	1.81	16.25	$\{4.2, \pi/2 - 0.1\}$	$\{0.921532, 0.0, -1.93\}$
RKA3	0.9	2.0	2.2	18.1	$\{4.0, \pi/2 - 0.2\}$	$\{0.638604, 0.0, 1.565\}$
RKA8	0.9	1.0	1.24	5.0	$\{3.0, \pi/2\}$	$\{1.15912, 0.497, 0.365\}$

Appendix D: Discrete Hamiltonian integrator

Starting from Equation (12) and considering a particle in electrovacuum, i.e., without the influence of the Lorenz force, the Hamiltonian reduces to

$$H(x^i, u_j) = \alpha \sqrt{1 + \gamma^{lm} u_l u_m} - \beta^r u_r. \quad (\text{D.1})$$

From the above expression, considering axisymmetry and Kerr-Schild coordinates, the discretized Hamiltonian equations can be written as (Bacchini et al. 2018):

Table C.2: Numerical parameters for the hybrid integrator shown in Subsection 3.1.2. In the top rows of the table we report the simulation a.0, while in the bottom rows the two simulations a.995_1 and a.995_2. Starting from the left, we report: The integrator scheme, the associated $\Delta t_{\#}$ for the time integration, the value of the constraint $(\partial_t \tilde{H})_{\max}$ for the “Hyb1” case, and the value of the constraint \tilde{H}_{\max} for the “Hyb2” case.

Scheme	Δt_{RK4}	Δt_{Ham}	$(\partial_t \tilde{H})_{\max}$	\tilde{H}_{\max}
a.0				
RK4	0.05	-	-	-
Ham	-	1.0	-	-
Hyb1	0.08	1.0	1.5	-
Hyb2	0.5	1.0	-	10^{-15}
a.995_1, a.995_2				
RK4	0.05	-	-	-
Ham	-	0.1	-	-
Hyb1	0.05	0.1	0.5	-
Hyb2	0.05	0.1	-	10^{-12}

$$\begin{aligned}
\frac{r^{n+1} - r^n}{\Delta t} = & \frac{1}{6} \left\{ \alpha(r^{n+1}, \theta^n) \frac{\gamma^{rr}(r^{n+1}, \theta^n)[u_r^{n+1} + u_r^n] + 2\gamma^{r\varphi}(r^{n+1}, \theta^n)u_{\varphi}^n}{\sqrt{1 + \xi_r^{n+1}(u_r^{n+1}, u_{\theta}^n, u_{\varphi}^n) + \sqrt{1 + \xi_r^n(u_r^n, u_{\theta}^n, u_{\varphi}^n)}} - \beta^r(r^{n+1}, \theta^n) \right. \\
& + \alpha(r^{n+1}, \theta^{n+1}) \frac{\gamma^{rr}(r^{n+1}, \theta^{n+1})[u_r^{n+1} + u_r^n] + 2\gamma^{r\varphi}(r^{n+1}, \theta^{n+1}, \varphi^{n+1})u_{\varphi}^{n+1}}{\sqrt{1 + \xi_r^{n+1}(u_r^{n+1}, u_{\theta}^{n+1}, u_{\varphi}^{n+1}) + \sqrt{1 + \xi_r^n(u_r^n, u_{\theta}^{n+1}, u_{\varphi}^{n+1})}} - \beta^r(r^{n+1}, \theta^{n+1}) \\
& + \alpha(r^n, \theta^{n+1}) \frac{\gamma^{rr}(r^n, \theta^{n+1})[u_r^{n+1} + u_r^n] + 2\gamma^{r\varphi}(r^n, \theta^{n+1}, \varphi^{n+1})u_{\varphi}^{n+1}}{\sqrt{1 + \xi_r^{n+1}(u_r^{n+1}, u_{\theta}^{n+1}, u_{\varphi}^{n+1}) + \sqrt{1 + \xi_r^n(u_r^n, u_{\theta}^{n+1}, u_{\varphi}^{n+1})}} - \beta^r(r^n, \theta^{n+1}) \\
& + \alpha(r^{n+1}, \theta^n) \frac{\gamma^{rr}(r^{n+1}, \theta^n)[u_r^{n+1} + u_r^n] + 2\gamma^{r\varphi}(r^{n+1}, \theta^n, \varphi^{n+1})u_{\varphi}^{n+1}}{\sqrt{1 + \xi_r^{n+1}(u_r^{n+1}, u_{\theta}^n, u_{\varphi}^{n+1}) + \sqrt{1 + \xi_r^n(u_r^n, u_{\theta}^n, u_{\varphi}^{n+1})}} - \beta^r(r^{n+1}, \theta^n) \\
& + \alpha(r^n, \theta^n) \frac{\gamma^{rr}(r^n, \theta^n)[u_r^n + u_r^n] + 2\gamma^{r\varphi}(r^n, \theta^n, \varphi^n)u_{\varphi}^n}{\sqrt{1 + \xi_r^{n+1}(u_r^{n+1}, u_{\theta}^n, u_{\varphi}^n) + \sqrt{1 + \xi_r^n(u_r^n, u_{\theta}^n, u_{\varphi}^n)}} - \beta^r(r^n, \theta^n) \\
& \left. + \alpha(r^n, \theta^n) \frac{\gamma^{rr}(r^n, \theta^n)[u_r^n + u_r^n] + 2\gamma^{r\varphi}(r^n, \theta^n, \varphi^{n+1})u_{\varphi}^{n+1}}{\sqrt{1 + \xi_r^{n+1}(u_r^{n+1}, u_{\theta}^n, u_{\varphi}^n) + \sqrt{1 + \xi_r^n(u_r^n, u_{\theta}^{n+1}, u_{\varphi}^{n+1})}} - \beta^r(r^n, \theta^n) \right\}, \tag{D.2}
\end{aligned}$$

We have defined the following quantities for conciseness:

$$\begin{aligned}
\xi_i^n := & \gamma^{ii}(u_i^n)^2 + 2\gamma^{ij}u_i^n u_j^n + 2\gamma^{ik}u_i^n u_k^n + 2\gamma^{jj}(u_j^n)^2 \\
& + 2\gamma^{kk}(u_k^n)^2 + 2\gamma^{jk}u_j^n u_k^n, \tag{D.8}
\end{aligned}$$

$$\begin{aligned}
\xi_i^{n+1} := & \gamma^{ii}(u_i^{n+1})^2 + 2\gamma^{ij}u_i^{n+1} u_j^n + 2\gamma^{ik}u_i^{n+1} u_k^n + 2\gamma^{jj}(u_j^n)^2, \\
& + 2\gamma^{kk}(u_k^n)^2 + 2\gamma^{jk}u_j^n u_k^n, \tag{D.9}
\end{aligned}$$

$$\zeta_i^{n+1} := \gamma^{lm}(x^{i,(n+1)}, x^{l,(n+1)}, x^{m,(n+1)})u_l u_m, \tag{D.10}$$

$$\zeta_i^n := \gamma^{lm}(x^{i,(n)}, x^{l,(n)}, x^{m,(n)})u_l u_m. \tag{D.11}$$

Note that in Eqs. (D.5)–(D.6) the derivatives of the metric components are reported analytically, but they are replaced by the corresponding finite-difference expressions whenever the denominator is sufficiently large to avoid numerical issues. As an example, for the derivative $\partial_i \gamma^{lm}$ we use the approximation $\partial_i \gamma^{lm} \simeq [\gamma^{lm}(x^{i,(n+1)}) - \gamma^{lm}(x^{i,(n)})]/(x^{i,(n+1)} - x^{i,(n)})$. We introduce a threshold ε on the coordinate increment $x^{i,(n+1)} - x^{i,(n)}$ and compute the derivative analytically only when the denominator is smaller than ε , which we set to $\varepsilon = 10^{-10}$. The same prescription is applied to the derivatives $\partial_i \alpha$ and $\partial_i \beta^j$, in all the momentum equations.

$$\begin{aligned}
\frac{\theta^{n+1} - \theta^n}{\Delta t} = & \frac{1}{6} \left\{ \alpha(r^{n+1}, \theta^{n+1}) \frac{\gamma^{\theta\theta}(r^{n+1}, \theta^{n+1})[u_\theta^{n+1} + u_\theta^n]}{\sqrt{1 + \xi_\theta^{n+1}(u_r^{n+1}, u_\theta^{n+1}, u_\varphi^n)} + \sqrt{1 + \xi_\theta^n(u_r^{n+1}, u_\theta^n, u_\varphi^n)}} \right. \\
& + \alpha(r^n, \theta^{n+1}) \frac{\gamma^{\theta\theta}(r^n, \theta^{n+1})[u_\theta^{n+1} + u_\theta^n]}{\sqrt{1 + \xi_\theta^{n+1}(u_r^n, u_\theta^{n+1}, u_\varphi^n)} + \sqrt{1 + \xi_\theta^n(u_r^n, u_\theta^n, u_\varphi^n)}} \\
& + \alpha(r^n, \theta^n) \frac{\gamma^{\theta\theta}(r^n, \theta^n)[u_\theta^{n+1} + u_\theta^n]}{\sqrt{1 + \xi_\theta^{n+1}(u_r^n, u_\theta^{n+1}, u_\varphi^n)} + \sqrt{1 + \xi_\theta^n(u_r^n, u_\theta^n, u_\varphi^n)}} \\
& + \alpha(r^{n+1}, \theta^{n+1}) \frac{\gamma^{\theta\theta}(r^{n+1}, \theta^{n+1})[u_\theta^{n+1} + u_\theta^n]}{\sqrt{1 + \xi_\theta^{n+1}(u_r^{n+1}, u_\theta^{n+1}, u_\varphi^{n+1})} + \sqrt{1 + \xi_\theta^n(u_r^{n+1}, u_\theta^n, u_\varphi^{n+1})}} \\
& + \alpha(r^{n+1}, \theta^n) \frac{\gamma^{\theta\theta}(r^{n+1}, \theta^n)[u_\theta^{n+1} + u_\theta^n]}{\sqrt{1 + \xi_\theta^{n+1}(u_r^{n+1}, u_\theta^{n+1}, u_\varphi^n)} + \sqrt{1 + \xi_\theta^n(u_r^{n+1}, u_\theta^n, u_\varphi^n)}} \\
& \left. + \alpha(r^{n+1}, \theta^n) \frac{\gamma^{\theta\theta}(r^{n+1}, \theta^n)[u_\theta^{n+1} + u_\theta^n]}{\sqrt{1 + \xi_\theta^{n+1}(u_r^{n+1}, u_\theta^{n+1}, u_\varphi^{n+1})} + \sqrt{1 + \xi_\theta^n(u_r^{n+1}, u_\theta^n, u_\varphi^{n+1})}} \right\}, \tag{D.3}
\end{aligned}$$

$$\begin{aligned}
\frac{\varphi^{n+1} - \varphi^n}{\Delta t} = & \frac{1}{6} \left\{ \alpha(r^{n+1}, \theta^{n+1}) \frac{2\gamma^{r\varphi}(r^{n+1}, \theta^{n+1})u_r^{n+1} + \gamma^{\varphi\varphi}(r^{n+1}, \theta^{n+1})[u_\varphi^{n+1} + u_\varphi^n]}{\sqrt{1 + \xi_\varphi^{n+1}(u_r^{n+1}, u_\theta^{n+1}, u_\varphi^{n+1})} + \sqrt{1 + \xi_\varphi^n(u_r^{n+1}, u_\theta^{n+1}, u_\varphi^n)}} \right. \\
& + \alpha(r^n, \theta^{n+1}) \frac{2\gamma^{r\varphi}(r^n, \theta^{n+1})u_r^n + \gamma^{\varphi\varphi}(r^n, \theta^{n+1})[u_\varphi^{n+1} + u_\varphi^n]}{\sqrt{1 + \xi_\varphi^{n+1}(u_r^n, u_\theta^{n+1}, u_\varphi^{n+1})} + \sqrt{1 + \xi_\varphi^n(u_r^n, u_\theta^{n+1}, u_\varphi^n)}} \\
& + \alpha(r^n, \theta^{n+1}) \frac{2\gamma^{r\varphi}(r^n, \theta^{n+1})u_r^n + \gamma^{\varphi\varphi}(r^n, \theta^{n+1})[u_\varphi^{n+1} + u_\varphi^n]}{\sqrt{1 + \xi_\varphi^{n+1}(u_r^n, u_\theta^{n+1}, u_\varphi^{n+1})} + \sqrt{1 + \xi_\varphi^n(u_r^n, u_\theta^{n+1}, u_\varphi^n)}} \\
& + \alpha(r^n, \theta^n) \frac{2\gamma^{r\varphi}(r^n, \theta^n)u_r^n + \gamma^{\varphi\varphi}(r^n, \theta^n)[u_\varphi^{n+1} + u_\varphi^n]}{\sqrt{1 + \xi_\varphi^{n+1}(u_r^n, u_\theta^n, u_\varphi^{n+1})} + \sqrt{1 + \xi_\varphi^n(u_r^n, u_\theta^n, u_\varphi^n)}} \\
& + \alpha(r^{n+1}, \theta^{n+1}) \frac{2\gamma^{r\varphi}(r^{n+1}, \theta^{n+1})u_r^{n+1} + \gamma^{\varphi\varphi}(r^{n+1}, \theta^{n+1})[u_\varphi^{n+1} + u_\varphi^n]}{\sqrt{1 + \xi_\varphi^{n+1}(u_r^{n+1}, u_\theta^{n+1}, u_\varphi^{n+1})} + \sqrt{1 + \xi_\varphi^n(u_r^{n+1}, u_\theta^n, u_\varphi^{n+1})}} \\
& \left. + \alpha(r^n, \theta^n) \frac{2\gamma^{r\varphi}(r^n, \theta^n)u_r^n + \gamma^{\varphi\varphi}(r^n, \theta^n)[u_\varphi^{n+1} + u_\varphi^n]}{\sqrt{1 + \xi_\varphi^{n+1}(u_r^n, u_\theta^n, u_\varphi^{n+1})} + \sqrt{1 + \xi_\varphi^n(u_r^n, u_\theta^n, u_\varphi^n)}} \right\}, \tag{D.4}
\end{aligned}$$

$$\begin{aligned}
\frac{u_r^{n+1} - u_r^n}{\Delta t} = & \frac{1}{6} \left\{ -\frac{1}{2} \left(\sqrt{1 + \zeta_r^{n+1}(u_r^n, u_\theta^n, u_\varphi^n)} + \sqrt{1 + \zeta_r^n(u_r^n, u_\theta^n, u_\varphi^n)} \right) \partial_r \alpha(r^{n+1}, \theta^n) + u_r^n \partial_r \beta^r(r^{n+1}, \theta^n) \right. \\
& - \frac{\left[\alpha(r^{n+1}, \theta^n) + \alpha(r^n, \theta^n) \right] \left[(u_r^n)^2 \partial_r \gamma^{rr}(r^{n+1}, \theta^n) + (u_\theta^n)^2 \partial_r \gamma^{\theta\theta} + (u_\varphi^n)^2 \partial_r \gamma^{\varphi\varphi} + 2u_r^n u_\varphi^n \partial_r \gamma^{r\varphi} \right]}{2 \sqrt{1 + \zeta_r^{n+1}(u_r^n, u_\theta^n, u_\varphi^n)} + \sqrt{1 + \zeta_r^n(u_r^n, u_\theta^n, u_\varphi^n)}} \\
& - \frac{1}{2} \left(\sqrt{1 + \zeta_r^{n+1}(u_r^n, u_\theta^{n+1}, u_\varphi^{n+1})} + \sqrt{1 + \zeta_r^n(u_r^n, u_\theta^{n+1}, u_\varphi^{n+1})} \right) \partial_r \alpha(r^{n+1}, \theta^{n+1}) + u_r^n \partial_r \beta^r(r^{n+1}, \theta^{n+1}) \\
& - \frac{\left[\alpha(r^{n+1}, \theta^{n+1}) + \alpha(r^n, \theta^{n+1}) \right] \left[(u_r^n)^2 \partial_r \gamma^{rr}(r^{n+1}, \theta^{n+1}) + (u_\theta^{n+1})^2 \partial_r \gamma^{\theta\theta} + (u_\varphi^{n+1})^2 \partial_r \gamma^{\varphi\varphi} + 2u_r^n u_\varphi^{n+1} \partial_r \gamma^{r\varphi} \right]}{2 \sqrt{1 + \zeta_r^{n+1}(u_r^n, u_\theta^{n+1}, u_\varphi^{n+1})} + \sqrt{1 + \zeta_r^n(u_r^n, u_\theta^{n+1}, u_\varphi^{n+1})}} \\
& - \frac{1}{2} \left(\sqrt{1 + \zeta_r^{n+1}(u_r^{n+1}, u_\theta^{n+1}, u_\varphi^{n+1})} + \sqrt{1 + \zeta_r^n(u_r^{n+1}, u_\theta^{n+1}, u_\varphi^{n+1})} \right) \partial_r \alpha(r^{n+1}, \theta^{n+1}) + u_r^n \partial_r \beta^r(r^{n+1}, \theta^{n+1}) \\
& - \frac{\left[\alpha(r^{n+1}, \theta^{n+1}) + \alpha(r^n, \theta^{n+1}) \right] \left[(u_r^{n+1})^2 \partial_r \gamma^{rr}(r^{n+1}, \theta^{n+1}) + (u_\theta^{n+1})^2 \partial_r \gamma^{\theta\theta} + (u_\varphi^{n+1})^2 \partial_r \gamma^{\varphi\varphi} + 2u_r^{n+1} u_\varphi^{n+1} \partial_r \gamma^{r\varphi} \right]}{2 \sqrt{1 + \zeta_r^{n+1}(u_r^{n+1}, u_\theta^{n+1}, u_\varphi^{n+1})} + \sqrt{1 + \zeta_r^n(u_r^{n+1}, u_\theta^{n+1}, u_\varphi^{n+1})}} \\
& - \frac{1}{2} \left(\sqrt{1 + \zeta_r^{n+1}(u_r^n, u_\theta^n, u_\varphi^{n+1})} + \sqrt{1 + \zeta_r^n(u_r^n, u_\theta^n, u_\varphi^{n+1})} \right) \partial_r \alpha(r^{n+1}, \theta^n) + u_r^n \partial_r \beta^r(r^{n+1}, \theta^n) \\
& - \frac{\left[\alpha(r^{n+1}, \theta^n) + \alpha(r^n, \theta^n) \right] \left[(u_r^n)^2 \partial_r \gamma^{rr}(r^{n+1}, \theta^n) + (u_\theta^n)^2 \partial_r \gamma^{\theta\theta} + (u_\varphi^n)^2 \partial_r \gamma^{\varphi\varphi} + 2u_r^n u_\varphi^n \partial_r \gamma^{r\varphi} \right]}{2 \sqrt{1 + \zeta_r^{n+1}(u_r^n, u_\theta^n, u_\varphi^{n+1})} + \sqrt{1 + \zeta_r^n(u_r^n, u_\theta^n, u_\varphi^{n+1})}} \\
& - \frac{1}{2} \left(\sqrt{1 + \zeta_r^{n+1}(u_r^{n+1}, u_\theta^n, u_\varphi^n)} + \sqrt{1 + \zeta_r^n(u_r^{n+1}, u_\theta^n, u_\varphi^n)} \right) \partial_r \alpha(r^{n+1}, \theta^n) + u_r^n \partial_r \beta^r(r^{n+1}, \theta^n) \\
& - \frac{\left[\alpha(r^{n+1}, \theta^n) + \alpha(r^n, \theta^n) \right] \left[(u_r^{n+1})^2 \partial_r \gamma^{rr}(r^{n+1}, \theta^n) + (u_\theta^n)^2 \partial_r \gamma^{\theta\theta} + (u_\varphi^n)^2 \partial_r \gamma^{\varphi\varphi} + 2u_r^{n+1} u_\varphi^n \partial_r \gamma^{r\varphi} \right]}{2 \sqrt{1 + \zeta_r^{n+1}(u_r^{n+1}, u_\theta^n, u_\varphi^n)} + \sqrt{1 + \zeta_r^n(u_r^{n+1}, u_\theta^n, u_\varphi^n)}} \\
& - \frac{1}{2} \left(\sqrt{1 + \zeta_r^{n+1}(u_r^n, u_\theta^{n+1}, u_\varphi^n)} + \sqrt{1 + \zeta_r^n(u_r^n, u_\theta^{n+1}, u_\varphi^n)} \right) \partial_r \alpha(r^{n+1}, \theta^n) + u_r^n \partial_r \beta^r(r^{n+1}, \theta^n) \\
& - \frac{\left[\alpha(r^{n+1}, \theta^n) + \alpha(r^n, \theta^n) \right] \left[(u_r^n)^2 \partial_r \gamma^{rr}(r^{n+1}, \theta^n) + (u_\theta^n)^2 \partial_r \gamma^{\theta\theta} + (u_\varphi^n)^2 \partial_r \gamma^{\varphi\varphi} + 2u_r^n u_\varphi^n \partial_r \gamma^{r\varphi} \right]}{2 \sqrt{1 + \zeta_r^{n+1}(u_r^n, u_\theta^{n+1}, u_\varphi^n)} + \sqrt{1 + \zeta_r^n(u_r^n, u_\theta^{n+1}, u_\varphi^n)}} \Big\}, \tag{D.5}
\end{aligned}$$

$$\begin{aligned}
\frac{u_\theta^{n+1} - u_\theta^n}{\Delta t} &= \frac{1}{6} \left\{ -\frac{1}{2} \left(\sqrt{1 + \zeta_\theta^{n+1}(u_r^{n+1}, u_\theta^n, u_\varphi^n)} + \sqrt{1 + \zeta_\theta^n(u_r^{n+1}, u_\theta^n, u_\varphi^n)} \right) \partial_\theta \alpha(r^{n+1}, \theta^n) + u_r^{n+1} \partial_\theta \beta^r(r^{n+1}, \theta^n) \right. \\
&\quad - \frac{[\alpha(r^{n+1}, \theta^{n+1}) + \alpha(r^{n+1}, \theta^n)] [(u_r^{n+1})^2 \partial_r \gamma^{rr}(r^{n+1}, \theta^n) + (u_\theta^n)^2 \partial_\theta \gamma^{\theta\theta} + (u_\varphi^n)^2 \partial_\theta \gamma^{\varphi\varphi} + 2u_r^{n+1} u_\varphi^n \partial_\theta \gamma^{r\varphi}]}{2 \sqrt{1 + \zeta_\theta^{n+1}(u_r^{n+1}, u_\theta^n, u_\varphi^n)} + \sqrt{1 + \zeta_\theta^n(u_r^{n+1}, u_\theta^n, u_\varphi^n)}} \\
&\quad - \frac{1}{2} \left(\sqrt{1 + \zeta_\theta^{n+1}(u_r^n, u_\theta^n, u_\varphi^n)} + \sqrt{1 + \zeta_\theta^n(u_r^n, u_\theta^n, u_\varphi^n)} \right) \partial_\theta \alpha(r^n, \theta^{n+1}) + u_r^n \partial_\theta \beta^r(r^n, \theta^{n+1}) \\
&\quad - \frac{[\alpha(r^{n+1}, \theta^{n+1}) + \alpha(r^n, \theta^n)] [(u_r^n)^2 \partial_r \gamma^{rr}(r^n, \theta^{n+1}) + (u_\theta^n)^2 \partial_\theta \gamma^{\theta\theta} + (u_\varphi^n)^2 \partial_\theta \gamma^{\varphi\varphi} + 2u_r^n u_\varphi^n \partial_\theta \gamma^{r\varphi}]}{2 \sqrt{1 + \zeta_\theta^{n+1}(u_r^n, u_\theta^n, u_\varphi^n)} + \sqrt{1 + \zeta_\theta^n(u_r^n, u_\theta^n, u_\varphi^n)}} \\
&\quad - \frac{1}{2} \left(\sqrt{1 + \zeta_\theta^{n+1}(u_r^n, u_\theta^{n+1}, u_\varphi^n)} + \sqrt{1 + \zeta_\theta^n(u_r^n, u_\theta^{n+1}, u_\varphi^n)} \right) \partial_\theta \alpha(r^n, \theta^{n+1}) + u_r^n \partial_\theta \beta^r(r^n, \theta^{n+1}) \\
&\quad - \frac{[\alpha(r^{n+1}, \theta^{n+1}) + \alpha(r^n, \theta^n)] [(u_r^n)^2 \partial_r \gamma^{rr}(r^n, \theta^{n+1}) + (u_\theta^{n+1})^2 \partial_\theta \gamma^{\theta\theta} + (u_\varphi^n)^2 \partial_\theta \gamma^{\varphi\varphi} + 2u_r^n u_\varphi^n \partial_\theta \gamma^{r\varphi}]}{2 \sqrt{1 + \zeta_\theta^{n+1}(u_r^n, u_\theta^{n+1}, u_\varphi^n)} + \sqrt{1 + \zeta_\theta^n(u_r^n, u_\theta^{n+1}, u_\varphi^n)}} \\
&\quad - \frac{1}{2} \left(\sqrt{1 + \zeta_\theta^{n+1}(u_r^{n+1}, u_\theta^n, u_\varphi^{n+1})} + \sqrt{1 + \zeta_\theta^n(u_r^{n+1}, u_\theta^n, u_\varphi^{n+1})} \right) \partial_\theta \alpha(r^{n+1}, \theta^{n+1}) + u_r^{n+1} \partial_\theta \beta^r(r^{n+1}, \theta^{n+1}) \\
&\quad - \frac{[\alpha(r^{n+1}, \theta^{n+1}) + \alpha(r^{n+1}, \theta^n)] [(u_r^{n+1})^2 \partial_r \gamma^{rr}(r^{n+1}, \theta^{n+1}) + (u_\theta^n)^2 \partial_\theta \gamma^{\theta\theta} + (u_\varphi^{n+1})^2 \partial_\theta \gamma^{\varphi\varphi} + 2u_r^{n+1} u_\varphi^{n+1} \partial_\theta \gamma^{r\varphi}]}{2 \sqrt{1 + \zeta_\theta^{n+1}(u_r^{n+1}, u_\theta^n, u_\varphi^{n+1})} + \sqrt{1 + \zeta_\theta^n(u_r^{n+1}, u_\theta^n, u_\varphi^{n+1})}} \\
&\quad - \frac{1}{2} \left(\sqrt{1 + \zeta_\theta^{n+1}(u_r^{n+1}, u_\theta^{n+1}, u_\varphi^{n+1})} + \sqrt{1 + \zeta_\theta^n(u_r^{n+1}, u_\theta^{n+1}, u_\varphi^{n+1})} \right) \partial_\theta \alpha(r^{n+1}, \theta^{n+1}) + u_r^{n+1} \partial_\theta \beta^r(r^{n+1}, \theta^{n+1}) \\
&\quad - \frac{[\alpha(r^{n+1}, \theta^{n+1}) + \alpha(r^{n+1}, \theta^n)] [(u_r^{n+1})^2 \partial_r \gamma^{rr}(r^{n+1}, \theta^{n+1}) + (u_\theta^{n+1})^2 \partial_\theta \gamma^{\theta\theta} + (u_\varphi^{n+1})^2 \partial_\theta \gamma^{\varphi\varphi} + 2u_r^{n+1} u_\varphi^{n+1} \partial_\theta \gamma^{r\varphi}]}{2 \sqrt{1 + \zeta_\theta^{n+1}(u_r^{n+1}, u_\theta^{n+1}, u_\varphi^{n+1})} + \sqrt{1 + \zeta_\theta^n(u_r^{n+1}, u_\theta^{n+1}, u_\varphi^{n+1})}} \Big\}, \tag{D.6}
\end{aligned}$$

$$\frac{u_\varphi^{n+1} - u_\varphi^n}{\Delta t} = 0. \tag{D.7}$$